Evaluation of reanalysis precipitable water vapor ~~estimates from three reanalysis datasets using ground-based GNSS, radiosonde, and radio occultation observations~~ under typhoon conditions using multi-source observations

Jiaqi Shi[1,2], Min Li[1,2], Andrea K. Steiner[3], Sebastian Scher[3,4], Minghao Zhang[5], Jiayu Hu[1,2], Wenliang Gao[1,2], Yongzhao Fan[1,2,6], and Kefei Zhang[5]

[1]GNSS Research Center, Wuhan University, Wuhan, 430079, China
[2]School of Geodesy and Geomatics, Wuhan University, Wuhan, 430079, China
[3]Wegener Center for Climate and Global Change, University of Graz, 8010 Graz, Austria
[4]Department of Geography and Regional Sciences, University of Graz, 8010 Graz, Austria
[5]School of Environmental Science and Spatial Informatics, China University of Mining and Technology, Xuzhou 221116, China
[6]School of Earth Sciences and Engineering, Hohai University, Nanjing, 211100, China

Correspondence to: Min Li (limin@whu.edu.cn)

Abstract. Precipitable ~~water~~ Water ~~vapor~~ Vapor (PWV) exhibits rapid and complex variations during typhoons, and its evaluation under typhoon conditions remains challenging due to sparse observations over the oceans. This study systematically evaluates PWV estimates from three state-of-the-art reanalyses during 113 typhoons between 2020 and 2024 over the Northwest Pacific and East Asia. The fifth-generation European Centre for Medium-Range Weather Forecasts Reanalysis (ERA5), the Modern-Era Retrospective Analysis for Research and Applications Version 2 (MERRA-2), and the Japanese Reanalysis for Three Quarters of a Century (JRA-3Q) are compared with ground-based Global Navigation Satellite System (GNSS), radiosonde~~s~~, and R~~r~~adio O~~o~~ccultation (RO) observations. Results based on ground-based GNSS, which serve as the primary reference in this study, ~~–~~show that ERA5 achieves the best overall accuracy~~provides the highest accuracy~~, with a bias changing from ~~of~~ −1.~~65~~ 48 mm in non-typhoon periods ~~and an even smaller bias of~~ to −0.~~29~~ 18 mm during typhoons~~,~~ and root mean square error (RMSE) decreasing from 3.~~52~~ 47 mm ~~in non-typhoon periods~~ to 3.30~~40~~ mm during typhoons. JRA-3Q also exhibits~~has~~ smaller error~~s~~ during typhoons ~~compared to~~than during non-typhoon periods, although its bias and RMSE remain relatively large. Conversely, MERRA-2 shows higher error during typhoons ~~compared to non-typhoon periods~~, with the bias shifting from ~~a modest underestimation of~~ −0.~~53~~ 63 mm in non-typhoon periods to ~~an overestimation of~~ 0.~~86~~ 76 mm during typhoons, indicating a transition from modest underestimation to modest overestimation~~but still maintains accuracy throughout typhoon periods~~. Comparisons with radiosonde and RO observations show consistently high correlations for all three reanalyses, supporting their general reliability under typhoon conditions. ~~PWV estimates from all three reanalyses show high correlations with those from radiosonde and RO observations.~~ Overall, the~~These~~ results provide an ~~comprehensive~~ accuracy reference during typhoons and support~~confirm~~ the

applicabilitysuitability of reanalyses reanalysis for PWV for typhoon-related studiesresearches during typhoons, with ERA5 appearing the most reliable robust among the datasets evaluated.

1 Introduction

Water vapor is primarily distributed within the troposphere and is one of the most important greenhouse gases. It plays a critical role in energy exchange within weather systems, the hydrological cycle, and climate change (e.g., Schneider et al., 2010; Sherwood et al., 2010). Precipitable water Water vapor Vapor (PWV), defined as the total amount of water vapor contained in a vertical column of the atmosphere per unit area, is a key variable for characterizing atmospheric water vapor. It is an important input parameter for Numerical Weather Prediction (NWP) models and is widely used in meteorological and climatological monitoring and forecasting (e.g., Zhao et al., 2020; Zhang et al., 2022). The spatio-temporal variation and distribution of PWV (also referred to as column water vapor) are related to the vertical structure of atmospheric moisture, tropical deep convection, and precipitation does not only influence the vertical humidity structure and water vapor transport processes but are also closely associated with the formation and development of various extreme weather events, including severe convective systems (Kim et al., 2022; Liu et al., 2023)(Muller et al., 2009; Holloway and Neelin, 2009).

Tropical cyclones Cyclones (TCs) are among the most destructive types of extreme weather. They occur frequently, exhibit high intensity, and cause widespread impacts (Emanuel, 2005; Walsh et al., 2012; Chan et al., 2018; Wang et al., 2020a; Shi et al., 2021; Xi et al., 2023). TCs are often accompanied by heavy rainfall and secondary disasters such as flooding, landslides, and debris flows (Woodruff et al., 2013; Cogan et al., 2018; Utsumi and Kim, 2022). Under a warming climateWith intensifying global warming, the average translationtranslational speed of TCs has been reported to decreased globally by approximately about 10% over 1949–2016. Meanwhile, TC precipitation rates are projected to increase, with a global median increase of approximately 14% across modelswhile their associated precipitation has increased by about 15%, which may contribute leading to more prolonged and damaging impacts in affected regions (Kossin, 2018; Elsner, 2020; Knutson et al., 2020) (Elsner, 2020; Intergovernmental Panel on Climate Change (IPCC), 2022; Tran et al., 2022). In the Northwest Pacific and the South China Sea, where TCs are referred to as typhoons, typhoons have frequently affected the Asia–Pacific region in recent years, including China, South Korea, and Japan, with southeastern China being particularly vulnerable and experiencing substantial casualties and economic losses

TCs occurring over the Northwest Pacific and the South China Sea are referred to as typhoons. In recent years, typhoons have frequently struck countries in the Asia Pacific region, including China, South Korea, and Japan, with southeastern China being particularly vulnerable. These events have resulted in substantial casualties and economic losses (Esteban and Longarte-Galnares, 2010; Jung et al., 2024; Wang et al., 2024). Some intense typhoons and their residual circulations have even penetrated deep into inland China. For example, Typhoon In-Fa (No. 2106) in 2021 and the double typhoons Doksuri (No. 2305) and Khanun (No. 2306) in 2023 caused record-breaking rainfall and devastatingsevere flooding in northern Henan province and Beijing–Tianjin–Hebei region innortheastern China (Shi et al., 2022; Zhao et al., 2024). Typhoons are

moisture-sensitive systems whose development depends strongly on the availability and transport of atmospheric water vapor. ~~As a type of extreme weather driven in part by atmospheric moisture, typhoons are strongly coupled with the spatio-temporal distribution of PWV.~~ PWV therefore provides an effective metric for depicting the pathways and strength of moisture transport during typhoons and for tracking moisture-related variations associated with their evolution and movement. ~~reveals the pathways and intensity of moisture transport during typhoons and exhibits a strong physical response to their evolution and movement.~~ Accordingly,~~Therefore,~~ high-accuracy PWV estimates are crucial for understanding the mechanisms underlying extreme precipitation during TCs, improving TC monitoring and forecasting, and supporting disaster risk assessment and mitigation efforts.

Various measurement techniques have been employed to retrieve PWV, including radiosondes, water vapor radiometers, satellite-based microwave/infrared remote sensing, and sun photometers (Ichoku et al., 2002; King et al., 2003; Li et al., 2003; Turner et al., 2007). In recent decades, advances in~~the development of~~ Global Navigation Satellite System (GNSS) technologies and Low Earth Orbit (LEO) satellites ~~has~~ have enabled the widespread application of ground-based GNSS and space-based GNSS ~~radio~~ Radio ~~occultation~~ Occultation (RO) for atmospheric observations (e.g., Melbourne et al., 1994; Kursinski et al., 1996; Li et al., 2017). However, these techniques have limitations when applied to~~, especially when applied to~~ fast-moving, ocean-based, and moisture-complex weather systems such as TCs, and obtaining ~~. Accurately estimating~~ PWV with both high resolution and temporal continuity remains challenging. In this context,

~~Conveniently,~~ gridded global reanalysis datasets provide atmospheric fields with high spatial and temporal resolution and no gaps, making it possible to obtain PWV at any time and location through interpolation. Reanalysis data ~~thus~~ therefore offer valuable resources for retrospectively investigating moisture transport and evolution during typhoons and for characterizing the spatio-temporal variability of atmospheric~~spatial and temporal features of~~ water vapor. Currently, several research institutions~~centers~~ provide atmospheric reanalysis datasets that are widely used, including the fifth-generation European Centre for Medium-Range Weather Forecasts (ECMWF) Reanalysis (ERA5) (Hersbach et al., 2020) ~~(Hersbach et al., 2020a)~~, the Modern-Era Retrospective Analysis for Research and Applications Version 2 (MERRA-2) (Gelaro et al., 2017) ~~(Gelaro et al., 2017a)~~, and the Japanese Reanalysis for Three Quarters of a Century (JRA-3Q) (Kosaka et al., 2024). Despite their broad use, the accuracy of reanalysis-based PWV can be affected by differences in data assimilation strategies and the underlying numerical models, as well as by the uneven spatio-temporal distribution of assimilated observations. Therefore, reanalysis-based PWV products should be systematically evaluated for accuracy and applicability before practical application.

~~Due to differences in data assimilation strategies and the uneven spatio-temporal distribution of assimilated observations, the accuracy of PWV estimates from reanalysis datasets remains uncertain. Therefore, we perform a systematic and comprehensive evaluation to assess the accuracy and applicability of PWV products from reanalyses prior to practical application.~~

Previous studies have evaluated the accuracy of PWV estimates from reanalysis datasets across different regions. These evaluations commonly rely on independent observations, including ground-based GNSS, radiosondes, and GNSS RO, as

reference data. In particular, ground-based GNSS-PWV typically achieves high accuracy (within 1–2 mm) and is not assimilated into any of the three reanalysis datasets examined in this study, making it an independent and reliable reference for validation~~Ground-based GNSS-PWV, with high accuracy of typically within 1–2 mm, is not assimilated into any of the three reanalysis datasets examined in this study, making them independent and reliable reference data for validation~~ (Wang et al., 2020b; Li et al., 2025)~~ (Wang et al., 2020; Li et al., 2025)~~. However, because GNSS stations are sparsely distributed over the oceans, radiosonde and GNSS RO observations are often used as complementary validation sources.~~given the sparse coverage of GNSS stations over oceans, many studies have also employed radiosonde and GNSS radio occultation (RO) observations as complementary validation sources.~~

At the regional scale, ~~evaluations have shown that~~ ERA5 ~~achieves~~ generally achieves lower PWV errors (<1 mm) over China and ~~, outperforming~~ outperforms its predecessor ERA-Interim, with cross-validation using radiosonde data further supporting~~confirming~~ its reliability (Zhang et al., 2019a, b)~~ (Zhang et al., 2019; Zhang et al., 2019)~~. In India, ERA5 also clearly outperforms MERRA-2 in PWV monitoring (Rani and Singh, 2025). Over the southern Tibetan Plateau, multiple reanalysis products exhibit systematic positive biases in the seasonal PWV cycle, likely linked to the persistent wet bias in regional models (Wang et al., 2017). In the Arctic, ~~evaluations suggest that~~ the Copernicus Arctic Regional Reanalysis (CARRA) ~~provides accurate PWV estimates and~~ shows good agreement with radiosonde observations, ~~although~~ but with evident seasonal variability (Zhang et al., 2025). At the global scale, reanalysis PWV agrees well~~has shown good agreement~~ with GNSS, radiosonde, and RO observations (Zhang et al., 2018). However, considerable uncertainties remain in tropical and ~~southern~~ Southern ~~hemisphere~~ Hemisphere regions, particularly for PWV ~~in PWV~~ estimates from the National Center for Environmental Prediction/Department of Energy (NCEP/DOE) dataset (Vey et al., 2010). ~~Moreover, g~~Geographic and climatic factors have also been shown to influence the consistency between reanalysis and GNSS-derived PWV (Bock and Parracho, 2019). Among the various products, ERA5 generally performs better than others~~outperforms others~~, while a~~China's~~ newly released Chinese global reanalysis dataset, China Meteorological Administration-40 (CRA40), exhibits comparable performance to ERA5 in PWV estimation (Wang et al., 2020b; Li et al., 2025)~~ (Wang et al., 2020; Li et al., 2025),~~ However, as CRA40 data are not fully publicly available, it is not included in this study. GNSS RO data have also been used to compare ERA5 and MERRA-2 PWV estimates in tropical and subtropical regions (Johnston et al., 2021). Additionally, ~~recent studies have identified~~ humidity modeling discontinuities in ERA5 at 09:00 and 21:00 UTC have been reported, which introduce diurnal jumps in ~~zenith~~ Zenith Ttropospheric Ddelay (ZTD) and subsequently affect PWV estimations (Yuan et al., 2025).

Existing evaluation studies have primarily focused on long-term and large-scale averages, with limited systematic ~~assessment~~ evaluation of PWV accuracy from reanalysis datasets under extreme weather conditions such as typhoons. Moreover, comparative analyses of PWV estimation accuracy between typhoon and non-typhoon periods remain scarce.

Driven by this research gap, we provide a systematic evaluation of PWV estimates from ERA5, JRA-3Q, and MERRA-2 during typhoon events using ground-based GNSS, radiosonde, and RO data from January 2020 to December 2024 over the Northwest Pacific and East Asia region. The data and methods used in this study are introduced in Section 2. Section 3

presents the evaluation results, and Section 4 provides~~Sections 4 and 5 provide a discussion and~~ discussion and conclusions~~, respectively~~.

~~2 Data and methodology~~

2 Data and methodology

In this section, the ~~we introduce the~~ typhoon datasets, the three reanalyses, ~~as well as~~and the observational data from ground-based GNSS, ~~space-based GNSS RO, and~~ radiosondes, and RO used in this study are introduced. ~~We also outline the~~ The PWV retrieval method, data quality control procedures, and the spatio-temporal collocation~~co-location~~ strategy are also described. In addition, the evaluation metrics and their formulations are provided.

2.1 Typhoon data

The typhoon dataset used in this study is obtained from the International Best Track Archive for Climate Stewardship (IBTrACS), which provides a unified, publicly available best-track dataset by integrating historical and recent records from multiple operational agencies worldwide (https://www.ncei.noaa.gov/products/international-best-track-archive, last accessed: 12 December 2025) (Knapp et al., 2010; Gahtan et al., 2024)~~, are sourced from the typhoon track real-time release system, operated by the Zhejiang provincial department of water resources and the Zhejiang water resources information management center (https://typhoon.slt.zj.gov.cn/, last accessed: 27 August 2025).~~ IBTrACS includes key parameters such as TC-center position, time, maximum sustained wind speed, and wind radius, typically reported at 3- and 6-hour intervals. ~~The system provides typhoon center location, time, wind speed, and additional information, with a temporal resolution of 1–3 hours that becomes finer with increasing typhoon intensity.~~ According to IBTrACS, the reporting agency currently responsible for the Northwest Pacific is the Japan Meteorological Agency (JMA), therefore, the JMA-reported typhoon information is used in this study. Because most GNSS stations used in this study are located in China and the China Meteorological Administration (CMA) and JMA intensity classifications are broadly comparable, typhoon categories are assigned following the CMA classification scheme,~~The typhoon categories in this dataset follow the classification scheme of the China Meteorological Administration (CMA),~~ which defines six categories based on wind speed: tropical depression (~~TD,~~ 10.8–17.1 m/s), tropical storm (~~TS,~~ 17.2–24.4 m/s), severe tropical storm (~~STS,~~ 24.5–32.6 m/s), typhoon (~~TY,~~ 32.7–41.4 m/s), severe typhoon (~~STY,~~ 41.5–50.9 m/s), and super typhoon (~~Super TY,~~ ≥51.0 m/s). For simplicity, these are denoted as L1 to L6, respectively. In this study, L1 typhoons are not included since no ~~GNSS~~ stations are ~~co-located~~collocated with their tracks.

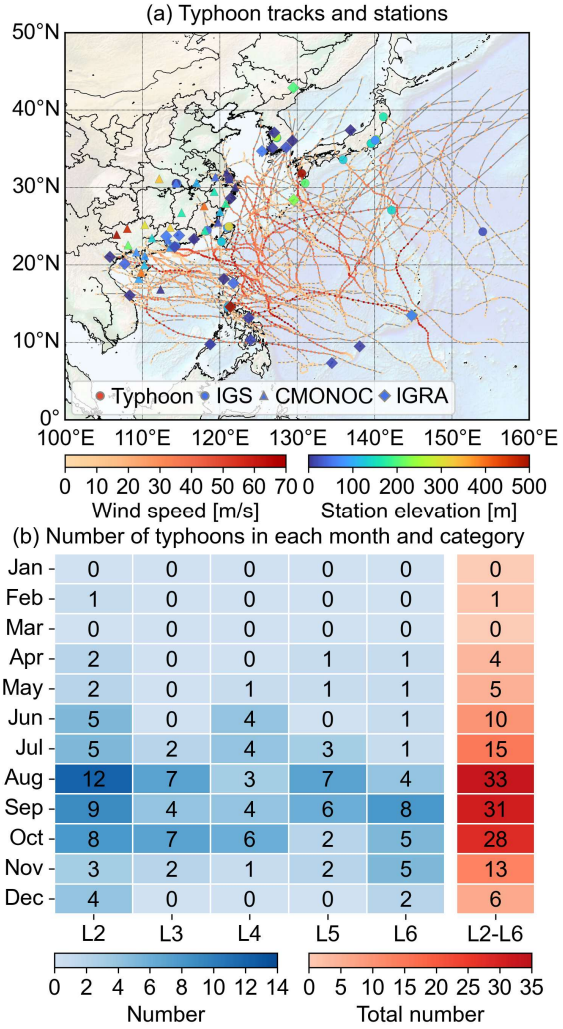

Figure 1~~:~~. (a) Spatial distribution of typhoon tracks, ground-based GNSS stations from IGS (marked by circles) and CMONOC (marked by triangles), and IGRA radiosonde stations (marked by diamonds) with colorbars indicating wind speed (in m/s, left) and station elevation (in m, right). (b) Number of typhoons in each month and category from January 2020 to December 2024.

There are 113 typhoons recorded from January 2020 to December 2024 ~~(This period represents the full extent of the available CMONOC dataset)~~, and the spatial distribution of their tracks is~~are~~ shown in Fig. 1a, together with the locations of the GNSS and radiosonde stations. Fig. 1b illustrates the number of typhoons by category over the five-year period, summed by month~~totaled per month~~. Typhoons occur most frequently from ~~July~~ June to November, with relatively higher counts in ~~the highest number of typhoons in~~ August, September, and October. ~~Specifically,~~The largest number of tropical storms (L2) ~~dominate~~ occurs in August, and the largest number of super ~~-~~typhoons (L6) occurs in September~~, while typhoon categories are more evenly distributed in October~~.

2.2 Reanalysis data

2.2.1 ERA5

ERA5 is the fifth generation of ECMWF reanalysis for ~~the~~ global climate and weather, providing a consistent record since 1940 and representing a state-of-the-art product developed by ECMWF~~for the past eight decades from 1940, and is a state-of-the-art reanalysis dataset developed by ECMWF~~ (Hersbach et al., 2020; Soci et al., 2024) ~~(Hersbach et al., 2020a; Soci et al., 2024b)~~. ERA5 is produced using an ensemble-based ~~four~~four-~~dimensional~~ dimensional ~~variational~~ variational (4D-Var) data assimilation system and model forecasts in CY41R2 of the ECMWF Integrated Forecast System (IFS), with 137 hybrid pressure levels in the vertical and the top level at 0.01 hPa. Atmospheric data are available on ~~the~~ interpolated 37 pressure levels. The native horizontal resolution is 0.25° × 0.25°, and the finest temporal resolution is ~~1~~ hourly.

2.2.2 MERRA-2

MERRA-2, developed by the Global Modeling and Assimilation Office (GMAO) at the National Aeronautics and Space Administration (NASA), provides global atmospheric reanalysis data starting from 1980 (Gelaro et al., 2017) ~~(Gelaro et al., 2017b)~~. Compared to its predecessor MERRA, MERRA-2 incorporates improvements in the Goddard Earth Observing System (GEOS) model and the Gridpoint Statistical Interpolation (GSI) assimilation system, enabling the assimilation of modern satellite observations such as hyperspectral radiance, microwave radiances~~microwave sensors~~, RO, and NASA ozone profiles. MERRA-2 ~~offers~~ has a horizontal resolution of 0.5° × 0.625°~~,~~ and 72 vertical levels up to 0.01 hPa, and the 3-hourly instantaneous data are used in this study~~instantaneous 3-hourly data are used in this study~~.

2.2.3 JRA-3Q

JRA-3Q is produced by the ~~Japan Meteorological Agency (~~JMA~~)~~ using ~~its~~ an advanced global ~~numerical weather prediction (~~NWP~~)~~ system to improve~~enhance~~ the quality and temporal coverage of long-term reanalysis (Kosaka et al., 2024). It builds ~~up~~on developments since JRA-55 and extending the record back to September 1947 and including many notable typhoon events.~~extends the reanalysis period back to September 1947, covering an earlier era that includes many notable typhoon events~~. JRA-3Q assimilates a wide range of reprocessed observational datasets, including rescued historical observations and satellite data provided by global meteorological and satellite centers. It employs a 4D-Var data assimilation system and addresses many of the limitations found in JRA-55, resulting in a high-quality and consistent dataset spanning over 75 years. The vertical structure includes 45 pressure levels, with a horizontal resolution of 0.375° × 0.375° and a temporal resolution of 6 hours. ~~It is noteworthy that the~~ JRA-3Q dataset was officially released in 2022, and related evaluation studies are still relatively limited. The evaluation conducted in this study may serve as a helpful reference for its future application.

Table 1 summarizes the data ~~centers~~providers, spatial and temporal resolutions, start time, update frequency, and assimilation strategies of the three reanalysis datasets. Further details can be found in the corresponding documentation ~~For~~

~~more detailed information, readers are referred to the publications~~ (Gelaro et al., 2017; Hersbach et al., 2020; Bell et al., 2021; Kosaka et al., 2024).

Table 1. Summary of three atmospheric reanalysis datasets used in this study.

Data description	ERA5~~ data on pressure levels~~	MERRA-2 ~~M2I3NVASM~~	JRA-3Q~~ isobaric analysis fields~~
Organizations	ECMWF	NASA GMAO	JMA
Horizontal resolution (lon × lat)	0.25°×0.25°	0.625°×0.5°	0.375°×0.375°
Vertical pressure levels	37	72	45
Temporal resolution	1-hourly	3-hourly	6-hourly
Temporal coverage	Jan 1940–present	Jan 1980–present	Sep 1947–present
Update frequency	Daily	Monthly	Monthly
Assimilation strategy	4D-Var	3D-Var	4D-Var

2.3 GNSS data

2.3.1 Ground-based GNSS data

Ground-based GNSS provides continuous, all-weather, high-precision observations of atmospheric variables with high temporal resolution, making it well-suited for evaluating reanalysis data under typhoon conditions. The International GNSS Service (IGS) provides ~~zenith~~ Zenith ~~path~~ Path ~~delay~~ Delay (ZPD, also known as ZTD) products at 5-minute intervals. However, most IGS stations in the Asia–Pacific region ~~is~~are~~ ~~ concentrated in Japan and South Korea, with sparse coverage along China's southeastern coast. To improve~~enhance~~ spatial coverage, GNSS data from~~we incorporate GNSS data from~~ the Crustal Movement Observation Network of China (CMONOC) are also used. These data are processed using the Position and Navigation Data Analyst (PANDA) software developed by Wuhan University (Shi et al., 2008), based on the Precise Point Positioning (PPP) technique (Zumberge et al., 1997), to generate ZTD estimates at the same temporal resolution as the IGS products. A ~~Additionally, a~~ quality control procedure is applied to exclude~~s~~ loosely constrained ZTD estimates, defined as those deviating from the station's monthly mean by more than four standard deviations ~~(STD)~~ (Zhang et al., 2017). ~~Fig. 1a shows the~~ The locations and elevations of IGS and CMONOC stations are shown in Fig. 1a~~and their elevation~~. To minimize errors in the vertical interpolation of PWV, ~~the analysis excludes~~ stations with elevations greater than 500 m are excluded. In total, ~~this study uses 34~~32 IGS and 29~~30~~ CMONOC stations are used in this study.

2.3.2 GNSS RO data

GNSS RO data of the Constellation Observing System for Meteorology, Ionosphere, and Climate-2 (COSMIC-2) mission, as the successor to COSMIC, are provided via the COSMIC Data Analysis and Archive Center (CDAAC) in Boulder, USA (Schreiner et al., 2020). The orbital inclination of the COSMIC-2 constellation is ~~specifically~~ designed to increase RO

sampling inenhance the number of RO observations over tropical and subtropical regions, and most profiles are resulting in nearly all RO profiles being distributed within a latitude range of 45°N to 45°S. Computing PWV estimation requires profiles of requires atmospheric specific humidity or water vapor partial pressure profiles. This study uses near-real-time wet profiles (hereafter "wetPrf") from the Level 2 products. The wetPrfs provide atmospheric parameters with a vertical sampling of 50 m below 20 km and 100 m between 20 km and 60 km (the upper limit of the profiles). These data are retrieved using a one-dimensional variational (1D-Var) technique, and the lowermost height varies among profiles (Wee et al., 2022). In tropical and subtropical regions, super-refraction can often prevents signals from penetrating to the surface, resulting in variations in the lowermost height across COSMIC-2 profiles (Schreiner et al., 2020; Wang et al., 2022). To reduce vertical interpolation errors, onlythis study uses only wetPrfs that pass the CDAAC quality control procedures and reach below 500 m are used in this study.

2.4 Radiosonde data

Radiosonde data used in this study are obtained from the Integrated Global Radiosonde Archive (IGRA), with routine observations conducted twice daily at approximately 0000 and 1200 UTC. PWV derived from radiosonde profiles typically has an uncertainty of 5% to 8% (Pérez-Ramírez et al., 2014; Turner et al., 2003). Despite certain limitations, radiosonde observations remain a standard reference for evaluating the PWV retrieved from other techniques (Gui et al., 2017). Quality control follows procedures describedis performed following the approaches proposed in previous studies (Wang and Zhang, 2008; Zhang et al., 2017), with additional criteria applied to ensure profile completeness and temporal coverage: (1) Profiles must reach at least 300 hPa, and only profiles with at least 30 vertical levels are used for PWV calculationHumidity profiles must extend to at least 300 hPa and include measurements at the surface and at a minimum of five standard pressure levels above the surface, regardless of whether surface pressure is above or below 1000 hPa.; (2) Profiles containing large data gaps, defined as pressure intervals exceeding 200 hPa between successive humidity measurements, are discarded; (3) Stations must operate continuously from January 2020 to December 2024, with at least 200 observations per year; (4) Stations with elevations exceeding 500 m are excluded (Shi et al., 2025). Only profiles with more than 30 vertical levels are used for PWV calculation. Based on these criteria, a total of 60 25 radiosonde stations isare retained for evaluation, and their. The locations of the radiosonde stations are indicated shown in Fig. 1.

2.5 Ground-based station selection scheme and RO co-location method

The gale force wind radius (R34, where 34 refers to wind speed in knots) is a key parameter for quantifying the spatial extent of a typhoon's impact. Previous studies report that R34 typically ranges from 210 km to 340 km (Sampson et al., 2017; Kim et al., 2022). In this study, the distance between each ground-based station and the typhoon center is calculated, and a station is considered to be in the typhoon area if the minimum distance is less than 300 km. For the comparison using RO profiles, spatio-temporal co-location with typhoon centers is required. Considering the horizontal smearing of RO profiles, a matching window of 100 km and 30 minutes is applied to associate RO profiles with corresponding typhoon centers.

2.~~6~~ 5 PWV estimation methods

PWV can be derived using two approaches. The first integrates specific humidity or water vapor partial pressure ~~profiles~~ and is applied to reanalysis, radiosonde, and RO data. The second converts the ~~zenith~~ Zenith ~~wet~~ Wet ~~delay~~ Delay (ZWD) estimated from GNSS PPP into PWV using a conversion factor.

2.~~6~~5.1 Reanalysis-PWV, radiosonde-PWV, and RO-PWV

The vertical integration for PWV can be expressed as follows:

$$PWV = \int_{p_1}^{p_2} \frac{q}{\rho_w \cdot g_s} dp \tag{1}$$

where p_1 and p_2 (in hPa) are the upper and lower pressure limits of the integration, respectively, q is the specific humidity (in g·kg^{-1}), , ρ_w is the density of liquid water, whose value is 1000 kg·m^{-3}, and g_s is the mean gravitational acceleration at the station. It is defined as:

$$g_s(\varphi, h) = g_n\left(1 - 0.0026373\cos(2\varphi) + 5.9 \cdot 10^{-6}\cos^2(2\varphi)\right) \cdot \left(1 - 3.14 \cdot 10^{-7} \cdot h\right) \tag{2}$$

where $g_n = 9.80665\ \mathrm{m \cdot s^{-2}}$ is standard acceleration of gravity, φ is latitude (in rad), h is elevation (in m). Specific humidity q can also be replaced by water vapor partial pressure e, with the conversion relationship as follows:

$$e = \frac{qp}{0.622 + 0.378q} \tag{3}$$

where p is pressure (in hPa).

2.~~6~~5.2 GNSS-PWV

The ZTD, comprising ~~zenith~~ Zenith ~~hydrostatic~~ Hydrostatic ~~d~~delay (ZHD) and ZWD, can be accurately estimated from GNSS observations using PPP, with ZHD precisely computed using the Saastamoinen model (Saastamoinen, 1972; Elgered et al., 1991):

$$\mathrm{ZHD} = \frac{0.002277 \cdot p_s}{1 - 0.00266 \cdot \cos(2\varphi) - 0.00028 \cdot H} \tag{4}$$

where φ is latitude (in rad) of the station, H is the ellipsoidal height of the station (in km). p_s represents the surface air pressure (in hPa). The ZWD is obtained by subtracting the ZHD from the ZTD:

$$\mathrm{ZWD} = \mathrm{ZTD} - \mathrm{ZHD} \tag{5}$$

the PWV can be obtained by multiplying ZWD by the water vapor conversion factor:

$$\mathrm{PWV} = \Pi \times \mathrm{ZWD} \tag{6}$$

where Π is the water vapor conversion factor, expressed as:

$$\Pi = \frac{1}{10^{-6}\rho_w R_v \left[\left(k_3 / T_m\right) + k_2'\right]} \tag{7}$$

where $\rho_w = 1000\ \mathrm{kg \cdot m^{-3}}$ is the density of liquid water, $R_v = 461.51\ \mathrm{J \cdot K^{-1} \cdot kg^{-1}}$ is the specific gas constant for water vapor, $k_2' = 17 \pm 10\ \mathrm{K \cdot hPa^{-1}}$ and $k_3 = 3.776 \pm 0.004 \times 10^5\ \mathrm{K^2 \cdot hPa^{-1}}$ are atmospheric refractivity constants, respectively. T_m denotes the weighted mean temperature, which can be determined using either an empirical linear model (Bevis et al., 1994) or by integration based on meteorological reanalysis data. It has been indicated in previous studies that calculating T_m using the integration method provides greater accuracy (Wang et al., 2005). The formula is presented as Eq. (8) (Davis et al., 1985; Bevis et al., 1992) ~~(Davis et al., 1985; Bevis et al., 1992)~~:

$$T_m = \frac{\int_{h_s}^{\infty}\left(e/T\right)dh}{\int_{h_s}^{\infty}\left(e/T^2\right)dh} = \frac{\sum_1^n \overline{\left(\frac{e_i}{T_i}\right)}\left(h_i - h_{i-1}\right)}{\sum_1^n \overline{\left(\frac{e_i}{T_i^2}\right)}\left(h_i - h_{i-1}\right)} \tag{8}$$

where e is the water vapor pressure at the station's zenith (in hPa), T is the temperature (in K), and h is the height (in m).

2.6 Data collocation schemes and PWV horizontal interpolation method

Wind radius can be used to characterize the spatial extent of a typhoon's influence. For the Northwest Pacific, recent IBTrACS records are primarily based on information from the JMA, which includes wind radius reported for different wind speed thresholds. In this study, a dynamic collocation scheme is adopted using the 30 kt wind radius to associate GNSS and radiosonde stations as well as RO profiles with the typhoon track. Specifically, the 30 kt wind radius includes the longest and shortest radius of 30 kt winds, and their mean is taken as the effective influence radius at each time. For GNSS and radiosonde observations, a station is considered collocated with the typhoon center when the distance between the station and the typhoon center is smaller than the time dependent effective radius. Temporally, the value at the target time is obtained by linear interpolation using the two observations closest in time. For RO profiles, a profile is regarded as collocated when the distance between the mean tangent point location and the typhoon center is smaller than the corresponding time dependent effective radius and the time difference does not exceed 30 minutes.

For PWV horizontal interpolation, bilinear interpolation is used. The target location is given by (lon, lat), where $lon \in [lon_1, lon_2]$, and $lat \in [lat_1, lat_2]$. The bilinear interpolation is expressed as:

$$\begin{cases} w_{lon} = \dfrac{lon - lon_1}{lon_2 - lon_1},\ w_{lat} = \dfrac{lat - lat_1}{lat_2 - lat_1} \\ \mathrm{PWV}(lon, lat) = (1 - w_{lon})(1 - w_{lat})\,\mathrm{PWV}_{11} + w_{lon}(1 - w_{lat})\,\mathrm{PWV}_{21} + (1 - w_{lon})\,w_{lat}\,\mathrm{PWV}_{12} + w_{lon} w_{lat}\,\mathrm{PWV}_{22} \end{cases} \quad (9)$$

where a w_{lon} and w_{lat} are the weights along the longitudinal and latitudinal directions, respectively. PWV_{11} donates the PWV value at (lon_1, lat_1), and PWV_{21}, PWV_{12}, and PWV_{22} are defined analogously at (lon_2, lat_1), (lon_1, lat_2), and (lon_2, lat_2).

~~**2.6.3 PWV vertical adjustment model**~~

~~To adjust PWV estimated from reanalyses to the height of GNSS or radiosonde stations, and to adjust RO PWV to the required height for comparison, a vertical adjustment is necessary. The exponential PWV adjustment model is currently widely used and computationally efficient, with the formula as follows:~~

~~$$PWV_1 = PWV_2 \exp\left(-(h_1 - h_2)/2\right) \quad (9)$$~~

~~where PWV_1 and PWV_2 represent the PWV at h_1 and h_2.~~

2.~~6.~~7 Statistical metrics

The statistical metrics used in this study include the systematic deviation of PWV from reanalysis with respect to observations, denoted as bias, Relative Bias (RB), ~~and~~ Root Mean Square Error~~root mean square error~~ (RMSE), and de-biased RMSE (dRMSE). The dRMSE represents the residual error after bias removal and is used to isolate the random component of PWV errors. They are calculated by the following formulas: ~~To provide a more intuitive representation of the PWV bias relative to the reference value, the relative bias (RB) is defined as follows:~~

$$\begin{cases} \mathrm{Bias} = \mathrm{PWV}_{reanalysis} - \mathrm{PWV}_{reference} \\ \mathrm{RB} = \dfrac{\mathrm{PWV}_{reanalysis} - \mathrm{PWV}_{reference}}{\mathrm{PWV}_{reference}} \times 100\% \\ \mathrm{RMSE} = \sqrt{\dfrac{1}{N}\sum_{i=1}^{N}\left(\mathrm{PWV}_{reanalysis,i} - \mathrm{PWV}_{reference,i}\right)^2} \\ \mathrm{dRMSE} = \sqrt{\dfrac{1}{N}\sum_{i=1}^{N}\left[\left(\mathrm{PWV}_{reanalysis,i} - \mathrm{PWV}_{reference,i}\right) - \overline{\mathrm{Bias}}\right]^2} \end{cases} \quad (10~~10~~)$$

where $PWV_{reanalysis}$ represents the PWV from different reanalysis data, and $PWV_{reference}$ is the reference PWV, which can be GNSS-PWV, radiosonde-PWV, or RO-PWV, $\overline{Bias}$ is the mean value of $Bias$.

In addition, to characterize the local spatial variability of reanalysis data, the Neighborhood Standard Deviation (NSD) is adopted as one of the evaluation metrics (Wei et al., 2013). NSD is used as a descriptive metric of subgrid scale spatial variability in reanalysis PWV around the target location. Larger NSD indicates stronger spatial heterogeneity within neighboring grid cells and thus a higher potential for representativeness mismatch when gridded fields are compared with point observations (Bock and Parracho, 2019). Because TCs are asymmetric and can exhibit sharp moisture gradients, high NSD does not necessarily imply a large reanalysis error, but provides context for interpreting the evaluation results under typhoon conditions. As illustrated in Fig. 7, NSD is computed at two spatial scales using the standard deviation of PWV from the 4 nearest grid points (NSD-4) and the 16 nearest grid points (NSD-16) around the typhoon center.

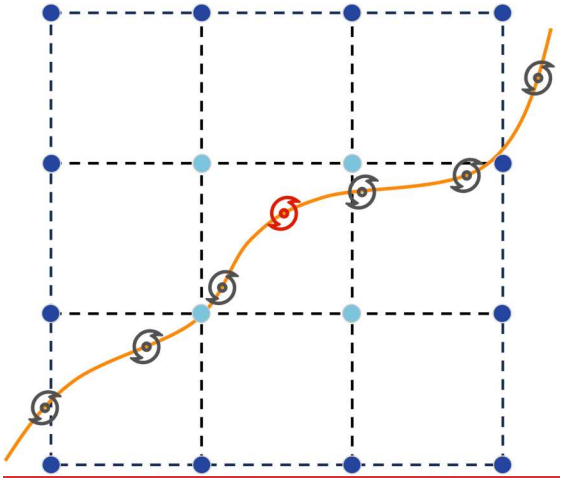

Figure 2. Schematic of NSD calculation. The orange line shows the typhoon track; the red marker indicates the typhoon center. The 16 nearest grid points are shown in dark blue and light blue, with the 4 closest points in light blue.

NSD-4 and NSD-16 can be calculated according to the following equation:

$$\begin{cases} \overline{\mathrm{PWV}} = \dfrac{1}{M}\sum_{j=1}^{M}\mathrm{PWV}_j \\ NSD = \sqrt{\dfrac{1}{M}\sum_{j=1}^{M}\left(\mathrm{PWV}_j - \overline{\mathrm{PWV}}\right)^2} \end{cases} \tag{11}$$

where $\overline{\mathrm{PWV}}$ denotes the mean PWV of the neighboring points, and M is set to 4 or 16.

3 Results

This section presents the evaluation results of PWV estimates from the three reanalysis datasets. For clarity ~~and consistency~~, prefixes are used to distinguish PWV derived from different data sources and their corresponding statistical ~~evaluation~~ metrics. Specifically, GNSS-PWV, RS-PWV, and RO-PWV denote PWV retrieved from ground-based GNSS, radiosonde, and RO data, respectively. For the reanalysis products, the initial letter of each dataset is used as a prefix. Accordingly, ~~Similarly,~~ E-PWV, M-PWV, and J-PWV refer to PWV estimated from ERA5, MERRA-2, and JRA-3Q ~~reanalysis datasets~~, respectively. ~~The term REA-PWV~~ The prefix "REA-" is used as a collective term for PWV estimates and associated statistical metrics derived from the three reanalysis datasets.~~collectively refers to all reanalysis-derived PWV values. The same naming convention is also applied to evaluation metrics such as bias and RMSE.~~

3.1 Evaluation using ground-based GNSS data

In this subsection, ~~For ground-based GNSS,~~ subscripts are used ~~when necessary~~ to distinguish results ~~data~~ from different GNSS networks when needed. Specifically, GNSS-PWV_I and GNSS-PWV_C ~~refer~~ denote ~~to~~ PWV estimated from IGS and CMONOC stations, respectively.

3.1.1 Monthly evaluation

To provide a comprehensive understanding of the PWV accuracy of the three reanalysis datasets, evaluations are conducted using data from 64 GNSS stations spanning January 2020 to December 2024. Monthly mean PWV from the reanalyses is compared to GNSS-PWV, with results shown in Fig. ~~2~~ 3. ~~The top, middle, and bottom rows of Fig. 2 display the monthly mean PWV (a1–a3), bias and RMSE (b1–b3), and RB (c1–c3), respectively. Red and yellow denote results referenced to GNSS-PWV_C, while blue and green correspond to GNSS-PWV_I.~~

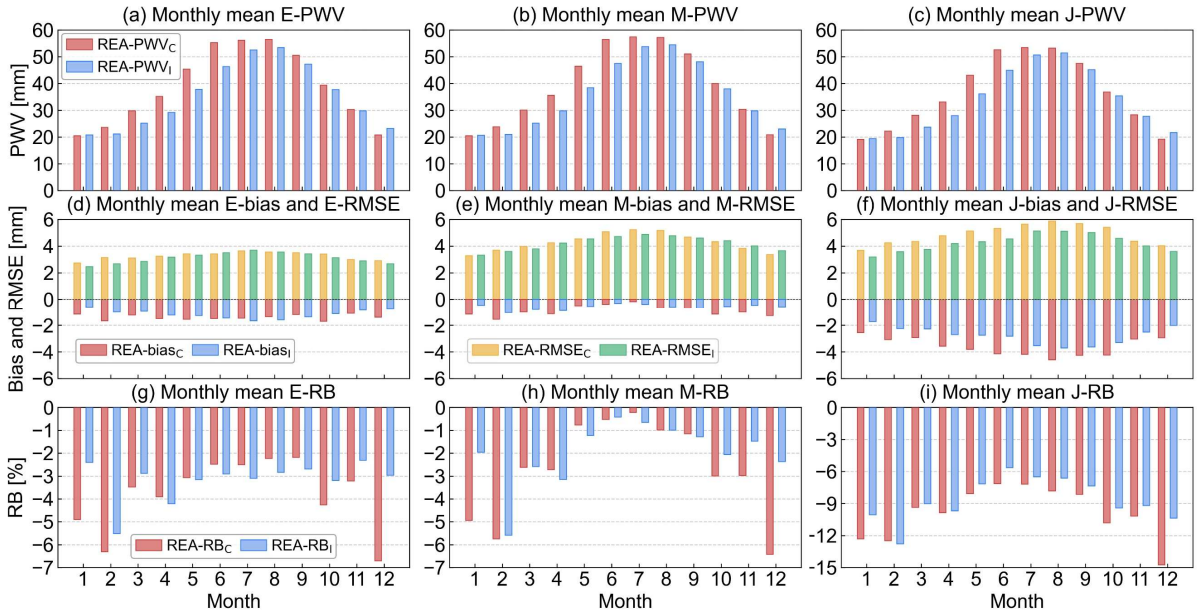

Figure ~~23:~~ . Monthly mean evaluation results. Panels (a-c) show REA-PWV (mm); red and blue bars denote REA-PWV sampled at the locations of CMONOC (REA-PWV$_C$) and IGS (REA-PWV$_I$) stations, respectively. Panels (d–f) show REA-bias and REA-RMSE (mm); red and yellow bars denote bias and RMSE at CMONOC stations (REA-bias$_C$ and REA-RMSE$_C$), respectively, and blue and green bars denote bias and RMSE at IGS stations (REA-bias$_I$ and REA-RMSE$_I$), respectively. Panels (g–i) show REA-RB (%); red and blue bars denote RB at CMONOC (REA-RB$_C$) and IGS (REA-RB$_I$) stations, respectively. Subscripts C and I indicate that reanalysis PWV is sampled at CMONOC and IGS station locations, respectively, and that the corresponding statistics (bias, RMSE, and RB) are computed against GNSS observations from the same network. ~~**Monthly mean evaluation results. (a1-a3) represent REA-PWV (in mm); (b1-b3) represent bias and REA-RMSE (in mm); (c1-c3) represent REA-RB. Red and yellow denote results referenced to GNSS-PWV$_C$, while blue and green correspond to GNSS-PWV$_I$.**~~

Monthly mean PWV from the three reanalyses (E-PWV, M-PWV, and J-PWV) show high consistency and pronounced seasonality in Fig. 3 (a–c), peaking at about 55 mm in July–August and dropping to about 20 mm in boreal winter. Notably, the PWV maximum slightly precedes the main typhoon season (August–October). REA-PWV$_C$ is generally higher than REA-PWV$_I$ from February to November but lower in the remaining months, mainly reflecting the different spatial distribution of GNSS stations from these two networks. Among the reanalyses, E-PWV and M-PWV are very similar, whereas J-PWV remains consistently lower than both E-PWV and M-PWV across all months. Biases in Fig. 3 (d–f) indicate that ERA5 and JRA-3Q have negative biases in every month (red and blue bars), with the absolute value of the bias positively correlated with PWV, consistent with previous studies indicating that mean REA-PWV is negatively biased in low-latitude regions (Wang et al., 2020b). The largest E-bias$_C$ and E-bias$_I$ occur in October and July (−1.70 mm and −1.66 mm), while the largest J-bias$_C$ and J-bias$_I$ both occur in August (−4.59 mm and −3.69 mm). In contrast, M-PWV agrees well with GNSS-PWV, with M-bias$_C$ and M-bias$_I$ remaining below 1 mm and approaching near-zero from May to September. RMSE (yellow and green bars in Fig. 3 (d–f)) follows a PWV-like seasonal cycle, with ERA5 having the smallest RMSE, followed by MERRA-2, and JRA-3Q the largest. RB in Fig. 3 (g–i) is smaller in summer and larger in winter, as expected

because it represents bias normalized by PWV, so its seasonality is largely governed by the PWV distribution and aligns with the bias pattern.

~~The monthly mean PWV from reanalyses, E-PWV, M-PWV, and J-PWV, exhibits high consistency and pronounced seasonal variation, with peaks of typically about 50 mm in July and August and low values of about 20 mm in boreal winter. The peak of PWV precedes the typhoon season, which occurs from August to October. Overall, GNSS-PWV$_C$ is generally higher than GNSS-PWV$_I$ from February to September, but lower in the other months. The monthly mean E-PWV and M-PWV are similar, while J-PWV remains consistently lower than both across all months. E-PWV and J-PWV show negative biases every month, with the absolute value of the bias positively correlated with PWV, consistent with previous studies indicating that mean REA-PWV is negatively biased in low-latitude regions (Wang et al., 2020). The largest E-bias$_C$ and E-bias$_I$ occur in October and July, with −1.82 mm and −1.63 mm, respectively, while the largest J-bias$_C$ and J-bias$_I$ both occur in August with −4.51 mm and −3.79 mm, respectively, from the GNSS ground-based observation. M-PWV shows good consistency with GNSS-PWV, with M-biases staying below 1 mm to near zero from May to September, when PWV is relatively high. The monthly mean RMSE follows a similar distribution pattern as PWV, with E-RMSE being the smallest, followed by M-RMSE, and J-RMSE being the largest. RB values are generally smaller in summer and larger in winter. When monthly mean PWV exceeds 40 mm (May to September), despite larger biases, RB remains below 3%.~~

For the months with more than ten typhoons within the five-year period (June to November), network-weighted mean bias and RMSE are obtained by combining the CMONOC- and IGS-based results, with weights determined by each network's proportion of the total number of used GNSS stations.~~For the months with more than ten typhoons within the five-year period (July to November), the weighted mean bias and RMSE are calculated based on the number of CMONOC and IGS stations~~. The resulting E-bias, M-bias, and J-bias are −1.~~38~~26 mm, −0.~~58~~73 mm, and −3.16~~74~~ mm, respectively, while the E-RMSE, M-RMSE, and J-RMSE are 3.~~38~~18 mm, 4.~~51~~25 mm, and ~~5.10~~4.55 mm, respectively (not shown). Among the three datasets, ~~Merra~~MERRA-2 shows the smallest~~least~~ systematic deviation, whereas~~while~~ ERA5 yields~~shows~~ the lowest RMSE, suggesting greater stability for E-PWV. For JRA-3Q, both the absolute value of J-bias and J-RMSE are the largest among the three reanalyses in most months.~~,~~ The next section presents a more detailed evaluation of REA-PWV ~~during typhoon events~~under typhoon conditions.

3.1.2 Composite evaluation considering adjacent periods of typhoons

~~In general, t~~Typhoon monitoring agencies release typhoon data based on wind speed. Data recording begins or ends when the wind speed reaches or falls below a specified threshold. ~~However, i~~It has been found that water vapor plays a critical role in TC formation~~,~~. ~~High~~ high column water vapor appears near the pouch center and starts to increase about 42 hours prior to genesis, while a substantial increase in precipitation occurs within 24 hours before genesis (Wang, 2014; Wang and Hankes, 2016). Moreover, even after typhoon dissipation or passage, residual circulation can continue to exert influence (Duan et al., 2014). Therefore, in addition to the recorded typhoon period (hereafter "r-typhoon"), ~~we also evaluate the accuracy of~~ REA-

PWVs is also evaluated during the a onethree-dayweek adjacent Adjacent period Period (AP), defined as the week three days before and the three daysweek after r-typhoon.. A schematic of r-typhoon and AP is provided in the top panel of Fig. 4.

Results are presented in Fig. 3. A schematic of the timeline with r-typhoon and the AP is shown in the top panel of Fig. 3. When referring to AP with a duration of X days, it indicates a period covering X days before and after r-typhoon. Figure 3 (a1–c4) presents the results for ERA5, MERRA-2, and JRA-3Q, respectively, while Fig. 3 (a3) and (a4) indicate the number of station-typhoon pairs. On the x-axis, L2 to L6 represent different typhoon categories, "L2–6" denotes all typhoon categories, and "Non" refers to the mean results for the same stations and periods in non-typhoon years during 2020–2024. For example, in the case of typhoon Doksuri (July 21–29, 2023), "Non" refers to results from the same station and the same period in 2020, 2021, 2022, and 2024, when no typhoon occurred.

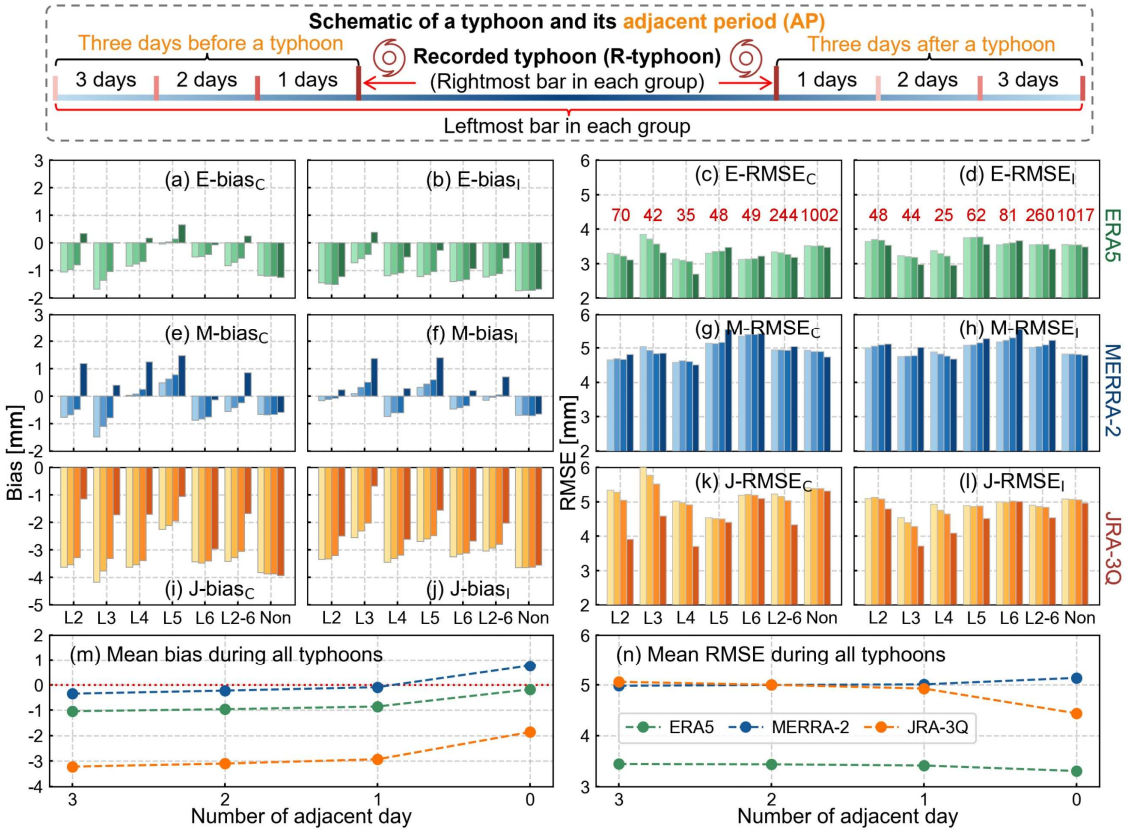

Figure 34.: The top panel shows a the schematic timeline of r-typhoon and the AP a typhoon, including the r-typhoon and AP. Panels (a–l) present biases and RMSEs under different AP settings across typhoon categories (ERA5: a-d; MERRA-2: e-h; JRA-3Q: i-l). Within each bar cluster, color from light to dark correspond to AP±3, AP±2, AP±1 days, and r-typhoon, respectively. "L2-6" and "Non" denote the results for all typhoons and for non-typhoon periods, respectively. Panels (c) and (d) report the numbers of CMONOC and IGS station–typhoon pairs. Panels (m) and (n) summarize the mean bias and RMSE averaged over all typhoons as a function of AP.

The bottom panel presents REA biases and REA-RMSEs (in mm) for different typhoon categories, with AP ranging from 7 days before/after to 0 day (color from light to dark). The x-axis shows typhoon categories or conditions. Panels (a3) and (a4) show the number of station-typhoon pairs, while (d1) and (d2) display the mean REA biases and REA-RMSEs for all typhoons.

~~For biases (Fig. 3, left panels), all three REA-biases generally decrease as the AP shortens. Specifically, the absolute values of E-bias and J-bias decrease, while that of M-bias increases. E-bias$_C$ and E-bias$_I$ (except during L6 typhoons) tend to decrease as AP shortens. For L2–L4 typhoons, both E-bias$_C$ and E-bias$_I$ change from negative to positive as AP shortens, with this effect most pronounced for E-bias$_C$ during L5 typhoons. According to Fig. 3 (d1), all E-biases are smaller than 1 mm, indicating good agreement between E-PWV and GNSS-PWV even when the bias turns positive. M-bias is predominantly positive and becomes more pronounced as AP shortens, though the mean bias for all typhoons remains within 1 mm. For L3 typhoons, the M-bias$_C$ exceeds 2.5 mm, which may be due to the limited sample size of only four events. All J-biases are negative. For L3 and L6 typhoons, J-bias$_C$ does not decrease monotonically as AP shortens. Overall, the absolute value of J-bias is the largest. Figure 3 (d1) shows that both E-bias and J-bias decrease as AP shortens, with values within r-typhoon of −0.21 mm and −1.89 mm, respectively. The absolute value of M-bias decreases from 7 adjacent days to 3 adjacent days, but becomes positive and increases when the AP is less than 3 days.~~

~~For RMSE (Fig. 3, right panels), both E-RMSE and J-RMSE tend to decrease with a shorter AP, especially for E-RMSE in L4 typhoons and J-RMSE in L2 and L4 typhoons. M-RMSE$_C$ shows no clear pattern with AP changes, whereas M-RMSE$_I$ generally increases as AP shortens. According to Fig. 3 (d2), E-RMSE, M-RMSE, and J-RMSE for all-typhoon periods remain nearly unchanged with AP variations. M-RMSE and J-RMSE are similar near 5 mm, while E-RMSE is the lowest near 3.5 mm.~~

~~Under non-typhoon conditions, REA biases and REA-RMSEs remain nearly unchanged with varying AP. Without considering AP, E-bias, M-bias, and J-bias are −1.58 mm, −0.53 mm, and −3.69 mm, respectively; E-RMSE, M-RMSE, and J-RMSE are 3.51 mm, 4.73 mm, and 5.08 mm, respectively. Among the three datasets, ERA5 yields the lowest RMSE, MERRA-2 shows the smallest bias, while JRA-3Q exhibits the largest bias and large RMSE.~~

Fig. 4 (a–l) shows bar charts of REA-biases and REA-RMSEs under different AP settings and typhoon categories. Here, "Non" denotes the mean results for the same stations and calendar periods in non-typhoon years during 2020–2024; for example, for typhoon Doksuri in 2023, "Non" refers to the same stations and dates in 2020, 2021, 2022, and 2024, when no typhoon occurred. The magnitude of the REA-bias generally decreases as AP shortens from ±3 days to r-typhoon period, meaning that biases tend to move closer to zero or shift from negative to positive. For ERA5 and JRA-3Q, both E-bias and J-bias decrease overall with a shorter AP, and E-bias at CMONOC stations becomes slightly positive during r-typhoon period (Fig. 4(a, b, i, j)). In contrast, M-bias increases slightly as AP shortens and turns more clearly positive during r-typhoon period (Fig. 4(e, f)), with a larger absolute value than under the ±3-day AP. Under non-typhoon conditions, the "Non" group in Fig. 4(a, b, e, f, i, j) shows consistently negative REA-biases and no pronounced dependence on AP length. For RMSE, E-RMSE and J-RMSE exhibit a slight overall decrease as AP shortens (Fig. 4(c, d, k, l)), although this tendency is weak for E-RMSE computed at IGS stations. In addition, J-RMSE decreases more markedly with shorter AP for weaker typhoons (L2–L4; Fig. 4(k)). By contrast, M-RMSE during r-typhoon period is slightly higher than during AP (Fig. 4(g, h)), indicating slightly larger errors when only r-typhoon period is considered. Similar to the bias, RMSE under non-typhoon conditions shows no pronounced dependence on AP (the "Non" clusters in Fig. 4(c, d, g, h, k, l)).

When aggregated across all typhoons, E-bias and J-bias are smaller than those during non-typhoon periods regardless of whether AP is included (the two rightmost bar groups in Fig. 4(a, b, i, j)). The corresponding RMSEs are also slightly lower than their non-typhoon counterparts (the two rightmost bar groups in Fig. 4(c, d, k, l)). This indicates that E-PWV and J-PWV exhibit higher overall accuracy during typhoon periods than during non-typhoon periods. Moreover, as AP shortens, E-bias, J-bias, E-RMSE, and J-RMSE further decrease, indicating that r-typhoon-only evaluation shows smaller errors than evaluations that include AP. For MERRA-2, M-bias is negative and close to zero when AP spans ±1 to ±3 days, whereas it becomes positive during r-typhoon period, with a larger absolute value than that during non-typhoon periods (Fig. 4(e, f), two rightmost bar groups). Meanwhile, M-RMSE is slightly higher during typhoon periods than during non-typhoon periods and is consistently larger than E-RMSE, while remaining comparable to J-RMSE (comparison of the two rightmost bar groups in Fig. 4(g, h) with those in Fig. 4(c, d, k, l)). The summaries in Fig. 4(m, n) quantify these differences: during r-typhoon period, the mean E-bias, M-bias, and J-bias are −0.18 mm, 0.76 mm, and −1.86 mm, respectively, and the mean E-RMSE, M-RMSE, and J-RMSE are 3.30 mm, 5.13 mm, and 4.44 mm, respectively. Overall, E-PWV shows the best performance during r-typhoon periods. M-PWV shows a positive shift in bias, but the mean bias remains within 1 mm. J-PWV improves relative to non-typhoon periods, although a negative bias remains.

3.1.3 Evaluation during recorded typhoon periods

This section focuses on the accuracy of PWVs during r-typhoon from reanalyses, without considering AP. Table 2 presents mean REA-biases, REA-RMSEs and dRMSEs of all typhoons during both r-typhoon and non-typhoon. ~~In addition, to distinguish between systematic bias and random error, the de-biased RMSE (dRMSE) is introduced as a supplementary metric to reflect the random component after removing bias. It should be noted that dRMSE is used as a reference metric to understand the errors better, while bias and RMSE remain the primary metrics for subsequent evaluation.~~

Table 2. **Mean REA-bias, REA-RMSE, and REA-dRMSE (mm) during r-typhoon period and non-typhoon periods at all GNSS stations, aggregated over all typhoons.** ~~**Mean REA-biases, REA-RMSEs, and REA-dRMSEs (in mm) of all typhoons during r-typhoon and non-typhoon periods.**~~

Metrics	Reanalyses	R-typhoon	Non-typhoon
Bias	ERA5	–0.18~~29~~	–1.48~~65~~
	MERRA-2	0.76~~86~~	–0.63~~53~~
	JRA-3Q	–1.86~~92~~	–3.74~~61~~
RMSE	ERA5	3.30~~40~~	3.47~~52~~
	MERRA-2	5.13~~19~~	4.76~~74~~
	JRA-3Q	4.44~~61~~	5.13~~01~~
dRMSE	ERA5	2.72~~86~~	2.48~~58~~
	MERRA-2	4.42~~55~~	34.88~~01~~
	JRA-3Q	3.32~~57~~	2.79~~84~~

~~For biases, E-biases and J-biases during r-typhoon periods are smaller in comparison to the non-typhoon periods across all typhoon categories, while the M-bias is only smaller for the L4 category during r-typhoon. For all typhoons, the mean biases~~

~~during non-typhoon periods are −1.65 mm and −3.61 mm for E-bias and J-bias, respectively, and −0.29 mm and −1.92 mm during r-typhoon periods, respectively. M-bias changes from −0.53 mm to 0.86 mm, increasing in absolute value and shifting from negative to positive. These results indicate that the overall underestimation of E-PWV and J-PWV is alleviated during r-typhoon, while M-PWV shifts from underestimation during non-typhoon to overestimation during r-typhoon, with the overestimation being more evident for L2 and L3 typhoons.~~

~~For RMSEs, both E-RMSE and J-RMSE are generally lower during r-typhoon compared to non-typhoon, decreasing by 0.12 mm and 0.40 mm, respectively. In contrast, M-RMSE increases by 0.45 mm during r-typhoon. The REA-dRMSEs for all categories and individual typhoon levels are higher during r-typhoon compared to non-typhoon. These results indicate that E-RMSE is the lowest and least affected by typhoons, whereas M-PWV exhibits higher uncertainty during typhoons. Interestingly, the REA-dRMSEs for all categories and individual typhoon levels are higher during r-typhoon compared to non-typhoon, opposite to REA-RMSE, which is lower during r-typhoon. This shows that the larger REA-RMSEs during non-typhoon periods, especially for E-RMSEs and J-RMSEs, are not caused by an increase in random error – which is indeed decreasing – but by an increase in bias. Thus, during typhoons, for ERA5 and JRA-3Q, the random error is higher, but the bias is much lower, leading to lower overall error.~~

Based on the bias results in Table 2, E-bias and J-bias during r-typhoon period are both closer to zero than during non-typhoon periods, indicating reduced underestimation in E-PWV and J-PWV under typhoon conditions. Among the three reanalyses, E-bias is closest to zero. In contrast, M-bias is larger during r-typhoon period than during non-typhoon periods and changes sign from negative to positive. Even so, r-typhoon M-bias (0.76 mm) is smaller in absolute value than r-typhoon J-bias (−1.86 mm). During non-typhoon periods, all three reanalyses underestimate PWV (E-bias = −1.48 mm, M-bias = −0.63 mm, and J-bias = −3.74 mm), with MERRA-2 showing the smallest bias magnitude. During r-typhoon period, the underestimation in ERA5 and JRA-3Q is alleviated, whereas MERRA-2 shifts to a moderate overestimation.

The RMSE results further show that, relative to non-typhoon periods, E-RMSE and J-RMSE during r-typhoon period decrease by 0.17 mm and 0.69 mm, respectively, whereas M-RMSE increases by 0.37 mm. E-RMSE is also the smallest among the three reanalyses, indicating the lowest overall error for E-PWV during r-typhoon period, followed by J-PWV, while M-PWV shows comparatively larger uncertainty. Since RMSE reflects both systematic and random components of error, Table 2 also reports dRMSE to characterize the random component after removing the bias. The dRMSE results show that all three REA-dRMSEs are higher during r-typhoon period than during non-typhoon periods, indicating an overall increase in the random error component under typhoon conditions. Notably, for ERA5 and JRA-3Q in Table 2, RMSE decreases from non-typhoon periods to r-typhoon period while dRMSE increases, indicating that the lower RMSE during r-typhoon is mainly driven by a reduction in systematic bias, which offsets part of the increase in the random error component. Conversely, the larger RMSEs during non-typhoon periods are primarily associated with larger biases rather than larger random errors. Overall, Table 2 suggests improved performance for E-PWV and J-PWV during r-typhoon period, whereas MERRA-2 shows a sign change in bias and a modest increase in RMSE, although its bias magnitude remains smaller than that of JRA-3Q.

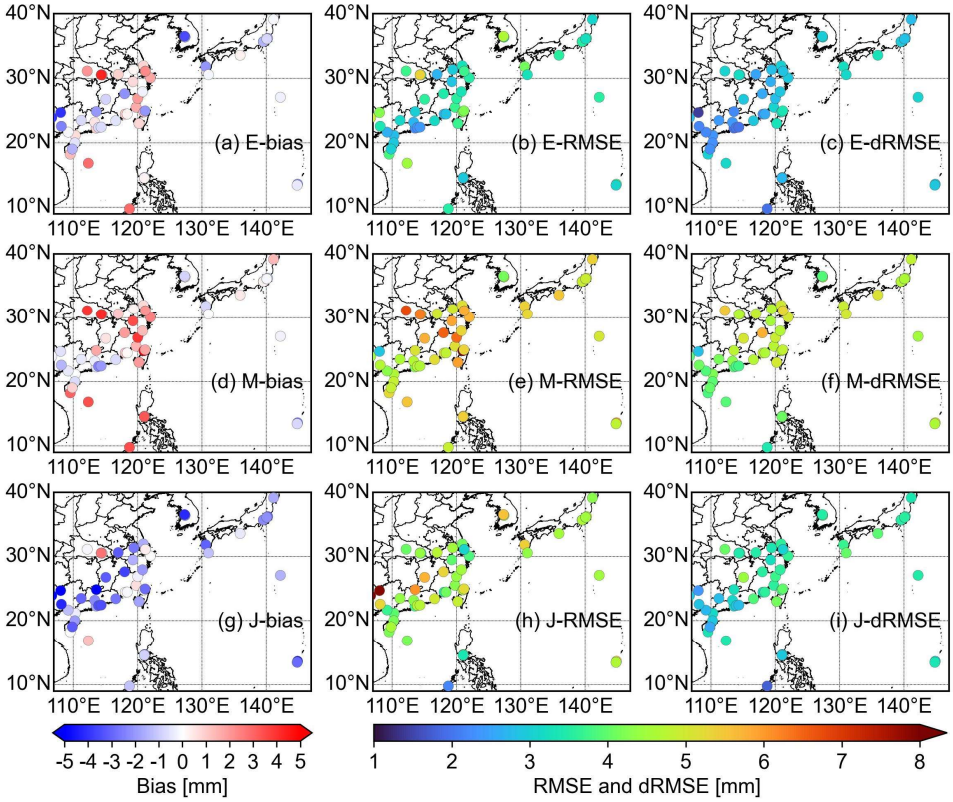

Figure 45: Spatial distribution of mean REA-biases, REA-RMSEs, and REA-dRMSEs (in mm) at GNSS stations during r-typhoon period, aggregated over all typhoons. ~~locations during r-typhoon for all typhoons.~~

~~Fig. 4 shows the spatial distribution of REA biases, REA RMSEs, and REA dRMSEs at GNSS stations during r-typhoon period for all typhoons. For biases, E-bias and M-bias exhibit similar spatial patterns: most stations in southern China and South Korea have negative biases, while those in eastern China are mainly positive. Notably, some stations in South China Sea, Philippines, Southern Japan also show prominent positive biases. J-bias is predominantly negative, with only a few stations showing positive values. For RMSE, E-RMSE is generally the lowest and most uniformly distributed, while M-RMSE is higher and shows relatively large values (>8 mm) at a station located in Southern Japan. J-RMSE falls between the other two, with the highest value (8.12 mm) observed at a station located in Fujian province, China. For dRMSE, E-dRMSE is the lowest overall, followed by J-dRMSE, while M-dRMSE is the highest and exhibits a clear latitudinal dependence, being larger at higher latitudes. Additionally, JRA-3Q displays the largest difference between RMSE and dRMSE among the three datasets, further indicating that the relatively large absolute J-biases substantially impact J-RMSE.~~

~~To sum up, E-PWVs and J-PWVs show improved accuracy during r-typhoon compared to non-typhoon, while M-PWVs exhibit a slight decrease in accuracy. However, the absolute value of mean M-bias remains within 1 mm, and its mean RMSE increases by only 0.45 mm. Despite some deterioration, M-PWVs still maintain a comparable level of accuracy~~

~~during typhoons. These results indicate that E-biases and J-biases are lower and their stability is better under the dynamic conditions of typhoons.~~

~~Nevertheless, the underlying causes of the changes in accuracy for all three REA PWVs during typhoons warrant further investigation. JRA-3Q assimilates JMA tropical cyclone bogus (TCB) data to improve the accuracy of typhoon analysis (Kosaka et al., 2024). This assimilation provides prior information on typhoons and helps constrain the estimation of atmospheric parameters, resulting in reduced J-bias and J-RMSE during typhoons. MERRA-2 does not assimilate any estimates of TC central surface pressures. Instead, TCs detected in the model background fields are relocated using the position given in the NCEP tcvitals reports following an established method (Liu et al., 2000; Koster et al., 2016), which enables MERRA-2 to more accurately capture typhoon processes. Despite this, M-PWV is generally overestimated and M-RMSE increases during typhoons.~~

~~Regarding RMSE, the reductions in E-RMSEs and J-RMSEs during r-typhoon are smaller than the corresponding improvements in E-biases and J-biases. This may be attributed to substantial atmospheric variability during typhoons, which maintains high random PWV uncertainties even with data assimilation. Overall, this study focuses on evaluating the accuracy of the three REA PWVs during typhoons, while the underlying causes of changes in their accuracy merit further investigation.~~

Fig. 5 shows the spatial distributions of REA-biases, REA-RMSEs, and REA-dRMSEs at GNSS stations during r-typhoon period for all typhoons. For the biases (Fig. 5(a, d, g)), E-bias exhibits both positive and negative values across stations and is overall closer to zero. In contrast, M-bias is predominantly positive, whereas J-bias is dominated by negative values (Fig. 5(d, g)), consistent with the earlier finding that M-bias shifts from negative to positive during r-typhoon period. Stations with positive E-bias and M-bias show some spatial similarity and are relatively concentrated in southern and southeastern China, while positive J-bias occurs at only a few stations. For the RMSEs (Fig. 5(b, e, h)), E-RMSE is generally the smallest and shows a comparatively homogeneous spatial distribution (Fig. 5(b)). M-RMSE is relatively low over southern China but exceeds 6 mm at a few stations in southeastern China (Fig. 5(e)). J-RMSE falls between E-RMSE and M-RMSE overall (Fig. 5(h)), with isolated stations showing comparatively large values (e.g., ~7.91 mm at GXHC), which may be related to the limited number of available stations–typhoon matchups, making the statistics more sensitive to individual events. For dRMSE (Fig. 5(c, f, i)), E-dRMSE remains the lowest, followed by J-dRMSE, whereas M-dRMSE is the largest and shows a latitudinal gradient, with larger values at higher latitudes. Notably, the difference between J-RMSE and J-dRMSE is comparatively pronounced (Fig. 5(h, i)), indicating a larger contribution of systematic bias to J-RMSE.

3.2 Evaluation using radiosonde observations

Although all three reanalyses assimilate radiosonde observations, RS-PWV is still used as a reference because of its high accuracy, to further evaluate REA-PWVs. Figure 6 compares REA-PWVs against RS-PWV across different typhoon stages and categories, including the 3 days before r-typhoon (pre-typhoon, Fig. 6(a)), r-typhoon (r-typhoon, Fig. 6(b)), and the 3 days after r-typhoon (post-typhoon, Fig. 6(c)), as well as r-typhoon results for individual categories (Fig. 6(d–h)). Figure 6(i)

provides the non-typhoon counterpart for comparison, and Fig. 6(j–k) summarizes the corresponding biases and RMSEs using bar charts. For convenience, E-r, M-r, and J-r denote the correlation coefficients (r) between RS-PWV and E-PWV, M-PWV, and J-PWV, respectively.

~~Although all three reanalysis datasets assimilate radiosonde observations, those observations are used as a reference due to their high accuracy, serving to further evaluate REA PWVs. Fig. 5 presents the evaluation results in terms of correlations between REA PWVs and RS PWVs. According to Fig. 5 (a–c), all three REA PWVs exhibit high agreement with RS PWVs during pre-typhoon, r-typhoon, and post-typhoon, especially for ERA5, whose correlation coefficients remain above 0.9. The correlation is slightly lower during pre-typhoon compared to r-typhoon and post-typhoon. Based on Fig. 5 (d–h), the correlation between REA PWVs and RS PWVs does not show notable variation across different categories, except for a noticeable decrease during L5 typhoons, where the correlation coefficients for ERA5 and MERRA-2 are below 0.9 and 0.8, respectively, and that for JRA-3Q also reaches its lowest value, 0.86.~~

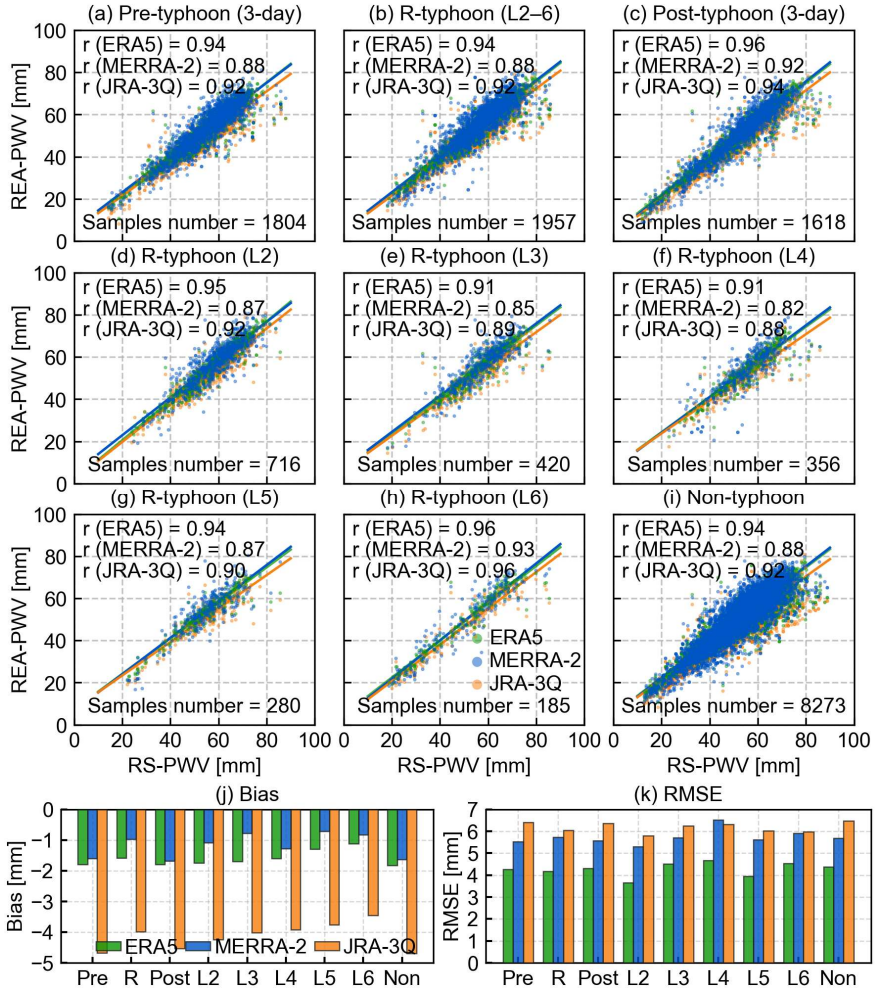

Figure 65.: Correlation statistics of REA-PWVs and RS-PWVs during for (a) pre-typhoon period (one week3 days before r-typhoon) (a), (b) r-typhoon period (b), (c)and post-typhoon period (one week3 days after r-typhoon) (c), (d–h)as well as during r-typhoon periods for different categories (d–h), and (i) non-typhoon periods. Panels (ji) and (kj) summarize the corresponding REA-biases and REA-RMSEs for panels (a–i)display bar charts of REA-biases and REA-RMSEs corresponding to Fig. 5 (a–h). Correlation coefficient (r) and the number of samples are shown in each panel (a–i)In the figure, "r" denotes the correlation coefficient, and the number of samples is also showed..

Comparing the three typhoon stages (Fig. 6(a–c)), E-r, M-r, and J-r are identical for pre-typhoon and r-typhoon periods, with E-r and J-r exceeding 0.9 and M-r equal to 0.88, consistent with the relatively larger M-RMSE during r-typhoon noted in Section 3.1. Correlations increase modestly in the post-typhoon period. For r-typhoon results stratified by typhoon category (Fig. 6(d–h)), all three correlations are higher for L2, L5, and L6 and lower for L3 and L4. Overall, E-r is the highest across categories and remains above 0.91; J-r is slightly lower and matches E-r during L6; M-r is generally the lowest but peaks during L6, reaching 0.93. Both J-r and M-r reach their minima during L4, at 0.82 and 0.88, respectively. When comparing the aggregated r-typhoon and non-typhoon results, E-r, M-r, and J-r are essentially the same, with values of 0.94, 0.88, and 0.92. To further quantify accuracy differences between r-typhoon and non-typhoon conditions, Table 2 reports the corresponding summary statistics, which align with the "R" and "Non" bar groups in Fig. 6(j–k).

Table 3. Mean REA-bias, REA-RMSE, and REA-dRMSE (mm) during r-typhoon and non-typhoon periods at all radiosonde stations, aggregated over all typhoons.

Metrics	Reanalyses	R-typhoon	Non-typhoon
Bias	ERA5	–1.95	–2.25
	MERRA-2	–1.35	–2.04
	JRA-3Q	–4.34	–5.12
RMSE	ERA5	6.29	6.50
	MERRA-2	7.43	7.41
	JRA-3Q	7.69	8.20
dRMSE	ERA5	5.98	6.10
	MERRA-2	7.31	7.13
	JRA-3Q	6.34	6.41

The conclusions drawn using RS-PWV as the reference are generally consistent with those based on GNSS-PWV. As shown in Table 3, during r-typhoon period, E-bias and J-bias are closer to zero than during non-typhoon period, decreasing by 0.30 mm and 0.78 mm, respectively. E-RMSE and J-RMSE are also smaller during r-typhoon period, with reductions of 0.21 mm and 0.51 mm. By contrast, M-RMSE is nearly unchanged between r-typhoon and non-typhoon periods, differing by only 0.02 mm. For dRMSE, M-dRMSE and J-dRMSE are slightly higher during r-typhoon period than during non-typhoon period, whereas E-dRMSE is slightly lower during r-typhoon period. It should be noted that the RS-PWV- and GNSS-PWV-based statistics do not always rank the three reanalyses in the same way. For example, during r-typhoon period, M-bias is the smallest among the three REA-biases. Such differences may be related to the relatively limited number of radiosonde observations and a smaller set of matched samples available for evaluation, which makes the statistics more sensitive to

individual samples. Therefore, the results in this section are best interpreted as complementary that supports the GNSS-referenced evaluation.

~~The results show that nearly all biases are negative, with positive M-biases observed only for L5 and L6 typhoons, both less than 0.3 mm. The absolute value of M-bias is the smallest, followed by E-bias, while J-bias has the largest absolute value. The mean REA biases during r-typhoon are lower than those during pre-typhoon and post-typhoon. For RMSE, E-RMSE is consistently the lowest, M-RMSE exceeds J-RMSE during L5 and L6 typhoons but is lower than J-RMSE for other categories. The variations of REA-RMSEs among pre-typhoon, r-typhoon, and post-typhoon are generally small. Notably, only J-RMSE increases by 0.3–0.5 mm in post-typhoon compared to pre-typhoon and r-typhoon. All three REA-RMSEs reach their lowest values during r-typhoon. Moreover, although the overall accuracy of J-PWV is lower than that of M-PWV, the correlation coefficients for J-PWV are higher than those for M-PWV in all cases (a–h), which may be due to systematic biases. These results indicate that all three REA-PWVs maintain strong correlations with RS-PWV under typhoon conditions.~~

3.3 Comparison with COSMIC-2 RO ~~profiles~~data

Evaluation using GNSS-PWV and RS-PWV as references is constrained by station locations, whereas RO-PWV can be used to compare REA-PWVs over the ocean. Based on the collocation scheme described in Section 2.6, 160 and 1299 COSMIC-2 RO profiles are collocated with typhoon centers during r-typhoon and non-typhoon periods, respectively, and these RO profiles are mainly distributed over the ocean. Given that only 160 samples are available during r-typhoon period, results stratified by typhoon category are not further reported in this section. Figure 7 shows the comparison results for (a) r-typhoon and (b) non-typhoon periods. During r-typhoon period, E-r, M-r, and J-r are 0.81, 0.77, and 0.80, respectively, which are lower than those during non-typhoon period by 0.09, 0.12, and 0.10. Table 4 further summarizes biases, RMSEs, and dRMSEs for r-typhoon and non-typhoon periods.

~~Evaluation using GNSS-PWVs and RS-PWVs as references is limited by station locations, whereas RO-PWVs can be used to compare REA-PWVs over oceanic regions. Based on the co-location scheme described in Section 2.5, there are 49 and 216 COSMIC-2 RO profiles co-located with typhoon centers during r-typhoon and non-typhoon, respectively. Fig. 6 presents the comparison results for r-typhoon and non-typhoon. REA-PWVs exhibit strong correlations with RO-PWV, with correlation coefficients of 0.92, 0.86, and 0.87 during r-typhoon. Overall, the correlation coefficients during r-typhoon are slightly lower than those during the non-typhoon.~~

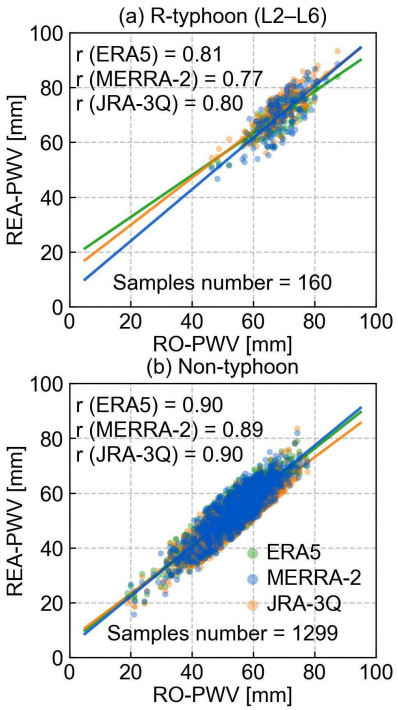

Figure ~~67:~~ . Correlation statistics of REA-PWVs and RO-PWVs ~~during~~ for (a) r-typhoon ~~(a)~~ and (b) non-typhoon periods ~~(b)~~. Correlation coefficients (r) and the number of samples are shown in each panel.~~In the figure, "r" denotes the correlation coefficient, and the number of samples is also showed.~~

Table 4. Mean REA-bias, REA-RMSE, and REA-dRMSE (mm) during r-typhoon and non-typhoon periods when compared with RO-PWV, aggregated over all typhoons.

Metrics	Reanalyses	R-typhoon	Non-typhoon
Bias	ERA5	1.27	−0.81
	MERRA-2	1.12	−0.55
	JRA-3Q	3.05	−2.64
RMSE	ERA5	4.12	4.02
	MERRA-2	5.17	4.32
	JRA-3Q	5.25	4.77
dRMSE	ERA5	3.92	3.94
	MERRA-2	5.05	4.28
	JRA-3Q	4.27	3.98

The error characteristics derived from comparisons with RO-PWV differ from those in the previous two sections, where GNSS-PWV and RS-PWV were used as references. During r-typhoon period, all three REA-biases are positive and are generally larger than those during non-typhoon period, indicating that the reanalyses tend to overestimate PWV relative to RO-PWV under typhoon conditions. Specifically, during r-typhoon period, E-bias and M-bias are 1.27 mm and 1.12 mm,

respectively, are comparable, whereas J-bias exceeds 3 mm. The REA-RMSEs are also larger during r-typhoon period than during non-typhoon period, suggesting increased overall uncertainty. In particular, M-RMSE and J-RMSE are 5.17 mm and 5.25 mm, respectively, exceeding E-RMSE by 1.05 mm and 1.13 mm. For dRMSE, M-dRMSE and J-dRMSE increase during r-typhoon period relative to non-typhoon period, whereas E-dRMSE decreases slightly. Overall, across both periods, MERRA-2 shows the smallest bias, while ERA5 yields the lowest RMSE. It should be noted that although more than 4,500 COSMIC-2 RO profiles are available per day in tropical and subtropical regions, the number of RO profiles used for comparison remains limited under the current collocation scheme. The differences between the RO-based results and those based on GNSS-PWV and RS-PWV may be related to the limited number of collocated samples and differences in land–ocean sampling, because most RO profiles used here are located over the ocean, whereas GNSS and radiosonde stations are mainly distributed over land. In addition, under typhoon influence, the water vapor field over the ocean tends to be more variable and spatially inhomogeneous, which may also contribute to larger discrepancies in this comparison.

~~**Table 3. REA biases and REA RMSEs relative to RO PWVs during r typhoon and non typhoon (in mm).**~~

	~~R typhoon~~		~~Non typhoon~~	
	~~Bias~~	~~RMSE~~	~~Bias~~	~~RMSE~~
~~ERA5~~	~~−0.45~~	~~2.85~~	~~−0.67~~	~~2.73~~
~~MERRA 2~~	~~0.67~~	~~4.05~~	~~−0.34~~	~~3.84~~
~~JRA 3Q~~	~~1.63~~	~~4.14~~	~~−2.45~~	~~4.03~~

~~Table 3 presents the biases and RMSEs of the three REA PWVs during the r typhoon and non typhoon periods. The absolute values of E bias and J bias are smaller by 0.22 mm and 0.82 mm during r typhoon compared to the non typhoon periods, respectively, while the absolute value of M bias increases by 0.33 mm. For RMSE, all three REA PWVs have higher values during r typhoon than in the non typhoon period, with increases of 0.12 mm, 0.21 mm, and 0.11 mm, respectively, indicating increased uncertainty in REA PWVs under typhoon conditions. Although there are more than 5,000 COSMIC 2 RO profiles per day in global tropical and subtropical regions, the number of co located RO profiles remains limited under the strict co location criteria. Therefore, the results in this section are intended primarily as complementary information.~~

3.4 ~~Neighborhood standard deviation~~Local spatial heterogeneity of REA-PWVs ~~of REA-PWVs~~

~~Neighborhood standard deviation (NSD) quantifies the local spatial variability of reanalysis data, reflecting the consistency among neighboring grid points (Wei et al., 2013). Higher NSD indicates stronger spatial heterogeneity and larger representativeness errors when comparing with point observations, which should be considered in evaluation (Bock and Parracho, 2019). NSD is particularly useful for characterizing spatial heterogeneity during extreme weather events such as typhoons, providing insights into the reliability of reanalysis products.~~

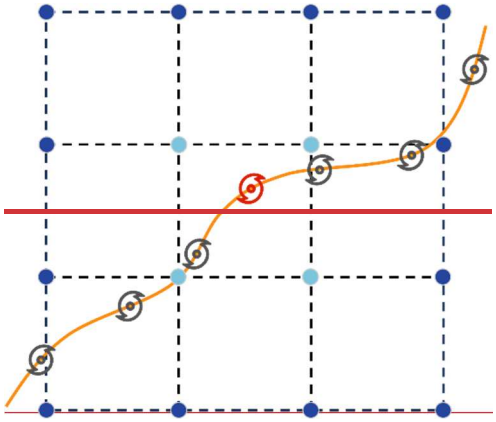

~~**Figure 7: Schematic of NSD calculation. The orange line shows the typhoon track; the red marker indicates the typhoon center. The 16 nearest grid points are shown in dark blue and light blue, with the 4 closest points in light blue.**~~

NSD is used to characterize the local spatial heterogeneity of gridded REA-PWVs and thus reflects the consistency among neighboring grid points. Comparing NSD between typhoon and non-typhoon periods helps quantify the complexity of PWV spatial structure under typhoon conditions. Table 5 summarizes NSD-16 and NSD-4 for the three REA-PWVs during r-typhoon and non-typhoon periods across all typhoon events.

Table 5. Mean NSD-16 and NSD-4 (mm) of three REA-PWVs during r-typhoon and non-typhoon periods over all typhoons.

NSD	Reanalyses	R-typhoon	Non-typhoon
NSD-16	ERA5	2.61	2.26
	MERRA-2	4.42	2.93
	JRA-3Q	2.21	1.60
NSD-4	ERA5	1.63	1.25
	MERRA-2	2.81	1.66
	JRA-3Q	1.25	0.85

~~To evaluate local spatial heterogeneity of the three REA-PWVs near typhoon centers, NSD is calculated at two scales based on the standard deviation of PWVs at the 16 nearest grid points (NSD-16) and at the 4 nearest grid points (NSD-4) around the typhoon center, as illustrated in Fig. 7. When calculating NSD, PWV at each grid point is interpolated to the altitude of the typhoon center.~~

According to Table 5, NSD-16 is generally larger than NSD-4 because it spans a broader neighborhood and includes more grid points, indicating that spatial variability is larger when evaluated over a broader neighborhood. Relative to non-typhoon periods, NSD increases for all three reanalyses during r-typhoon period, suggesting a more complex local PWV structure and stronger spatial inhomogeneity under typhoon conditions. Specifically, E-NSD-16, M-NSD-16, and J-NSD-16 increase by 15.5%, 50.9%, and 38.1%, respectively, while the corresponding increases for NSD-4 are larger, reaching 30.4%, 69.3%, and 47.1%. The relative increase is larger for NSD-4 than for NSD-16, indicating that NSD changes more strongly when evaluated at a smaller neighborhood scale. Systematic differences are also evident among the reanalyses. MERRA-2 exhibits the largest NSD at both scales and the strongest increase from non-typhoon to r-typhoon, whereas ERA5 and JRA-3Q show

lower NSD values and more moderate changes. It should be noted that NSD describes spatial variability of the local PWV field rather than PWV error itself. Therefore, higher NSD during r-typhoon period can be interpreted indicating stronger local spatial variability when comparing REA-PWVs.

~~For all typhoons under non typhoon conditions, E-NSD-16, M-NSD-16, and J-NSD-16 are 2.23, 2.85, and 1.59 mm, while E-NSD-4, M-NSD-4, and J-NSD-4 are 1.24, 1.61, and 0.84 mm, respectively. In both NSD-16 and NSD-4, J-NSD is the smallest, E-NSD is intermediate, and M-NSD the largest, indicating strongest spatial consistency for J-PWV and weakest for M-PWV. During r-typhoon periods, all NSDs increase: E-NSD-16, M-NSD-16, and J-NSD-16 rise to 2.61, 4.17, and 2.30 mm, representing relative increases of 17.1%, 46.4%, and 44.8%, while E-NSD-4, M-NSD-4, and J-NSD-4 rise to 1.62, 2.64, and 1.31 mm, corresponding to increases of 30.9%, 63.5%, and 56.2%. M-NSD shows the largest absolute and relative increases among the three reanalyses. Overall, the NSDs of the three REA-PWVs increase markedly during typhoons, indicating enhanced spatial heterogeneity under typhoon conditions. Despite this increase, E-NSD and J-NSD generally remain below 3 mm, while M-NSD stays within 5 mm.~~

~~A direct evaluation of the NSD is not possible, as NSD cannot be computed from the observations used in this study. However, the NSD results help in interpreting the results of the errors and biases of the reanalysis products. MERRA has the highest random error (dRMSE) of the three reanalysis datasets. An overestimation of NSD would lead to higher random error. Therefore, this suggests that the NSD of MERRA is overestimated, and the lower NSD of ERA and JRA is closer to the true values – which is in line with the lower dRMSE of ERA and JRA. This also explains why MERRA, despite having generally lower absolute bias levels compared to JRA, still has higher overall RMSE.~~

~~4 Discussion~~

~~Beyond the direct accuracy evaluation, a further aspect to consider is how typhoon center station distance (hereafter "distance") and wind speed may influence the performance of REA-PWVs, since these factors are not explicitly accounted for when comparing them with GNSS-PWVs. Therefore, this section further investigates the influence of these two parameters. Fig. 8 presents three representative typhoon–station pairs with minimum distances less than 200 km: In-fa–JSLS, Doksuri–KMNM, and Khanun–AIRA. To facilitate the discussion of water vapor related changes during each typhoon, precipitation obtained from the Global Precipitation Measurement (GPM) mission is also plotted (gray bars). The right panels show the corresponding time series of REA biases.~~

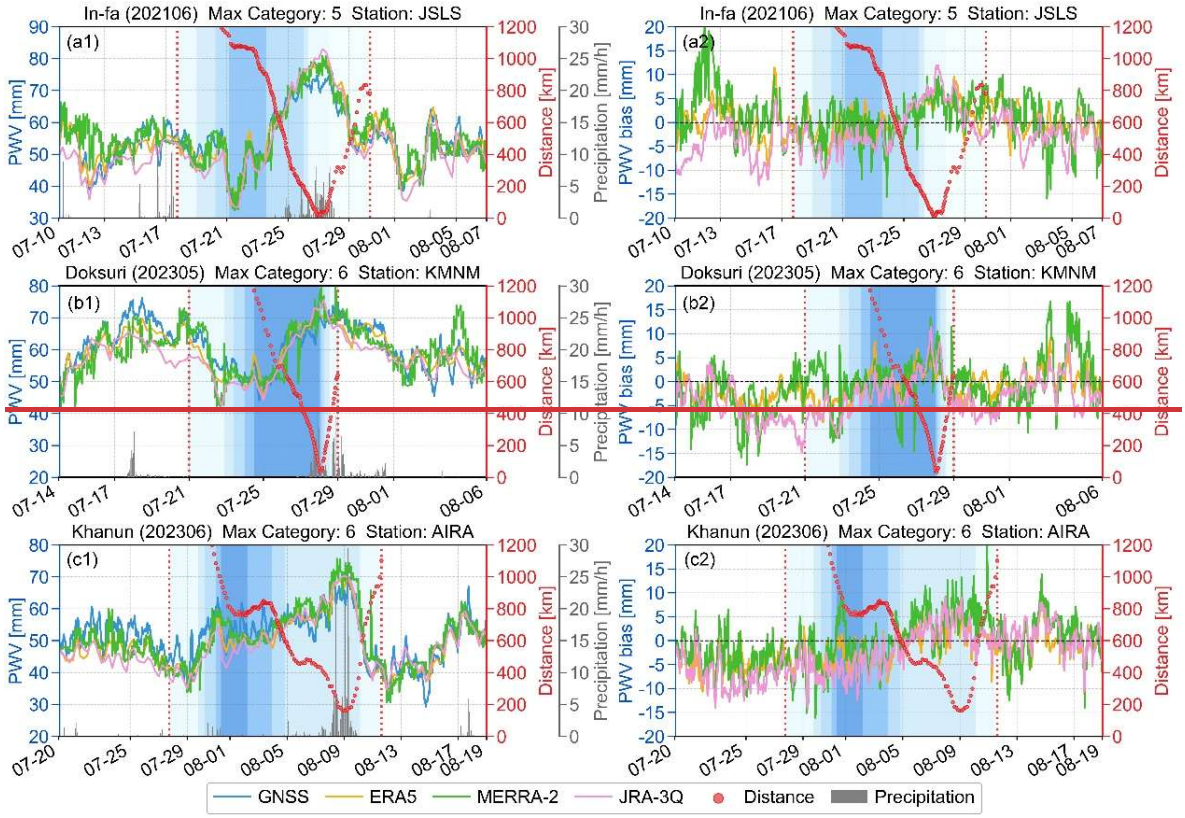

~~**Figure 8: Time series of PWVs and biases for three typhoon-GNSS station pairs. The left and right columns show PWVs and biases, respectively. PWVs and biases correspond to the left y-axis (in mm); distance to the right red y-axis (in km); and precipitation to the right gray y-axis (in mm/h). Vertical red dashed lines divide the series into pre-typhoon, r-typhoon, and post-typhoon periods. Each panel is annotated with the typhoon number, name, maximum category, and station. Blue shading of varying intensity (darker for stronger categories) indicates typhoon categories, and the x-axis shows month–day.**~~

~~According to Fig. 8 (a1–c1), all three REA PWVs demonstrate generally high consistency with GNSS PWVs. However, as shown in Fig. 8 (a2–c2), large absolute values of M biases, sometimes exceeding 10 mm and even approaching 20 mm, are observed during pre-typhoon of In-fa, post-typhoon of Doksuri, and r-typhoon of Khanun. Additionally, J biases during pre-typhoon also reach negative values less than −10 mm. In contrast, E biases perform better overall, with fewer occurrences of absolute biases greater than 10 mm. Analysis of the distance pattern reveals that when the distance gets below approximately 600 km, all three REA biases tend to shift from negative to positive, suggesting a certain correlation between REA biases and distance. On the other hand, no clear trend is observed in REA biases with changes in typhoon categories.~~

~~Further statistical analysis shows that during r-typhoon for all typhoons, the correlation coefficients between distance and E-bias, M-bias, and J-bias are −0.286, −0.202, and −0.370, respectively, indicating weak negative correlations. Meanwhile, the correlation coefficients with wind speed are all below 0.1, indicating no relationship. These results suggest that, when distance and wind speed are not explicitly considered, the evaluation of REA PWVs based on GNSS PWVs is generally reasonable and representative. Although neither distance nor wind speed show a clear correlation with PWV accuracy, the~~

~~influence of distance appears to be slightly stronger than that of wind speed. This analysis provides a preliminary understanding of the potential influence of distance and wind speed on the evaluation of REA PWVs. Future work may consider introducing multivariate approaches to enable more detailed evaluations.~~

~~5~~ 4 Discussion and c~~C~~onclusions

This study presents a systematic evaluation of PWV during typhoons from the ERA5, MERRA-2, and JRA-3Q reanalyses using three independent observational references: ground-based GNSS, radiosonde, and COSMIC-2 RO data. A total of 113 typhoon events from January 2020 to December 2024 are analyzed. The evaluation focuses on contrasts between typhoon and non-typhoon periods in bias, RMSE, and dRMSE, and further examines dependence on typhoon category when sample sizes permit.

~~This study provides the first systematic evaluation of the accuracy of PWV estimates from ERA5, MERRA-2, and JRA-3Q reanalysis datasets under typhoon conditions, using ground-based GNSS, radiosonde, and RO observations. More than 100 typhoon events from 2020 to 2024 are examined across four scenarios, namely pre-typhoon, r typhoon, post-typhoon, and adjacent periods, and results for each scenario are compared with the result during non-typhoon periods.~~

In the ground-based evaluations, GNSS provides higher temporal resolution and a larger sample size and is therefore used as the primary reference in this study. The radiosonde-based evaluation serves as an independent external check. Using GNSS-PWV as the reference, ERA5 shows the best overall performance under typhoon conditions, with the bias closest to zero and the lowest RMSE (−0.18 mm and 3.30 mm). M-bias lies between E-bias and J-bias, while M-RMSE is the largest among the three reanalyses. J-PWV exhibits a more pronounced negative bias, and J-RMSE falls between E-RMSE and M-RMSE. Relative to non-typhoon period, the absolute values of E-bias and J-bias decrease, indicating reduced mean systematic bias in E-PWV and J-PWV during typhoons. M-bias increases slightly but remains below 1 mm, suggesting that MERRA-2 maintains a bias level comparable to that in non-typhoon period. In terms of RMSE, E-RMSE and J-RMSE decrease by 0.17 mm and 0.69 mm during typhoon period, respectively. Together with the bias changes, this indicates an overall reduction in total error for E-PWV and J-PWV, whereas M-RMSE is higher during typhoon period than during non-typhoon period. By construction, dRMSE is no greater than RMSE, however, all three REA-dRMSEs are higher during typhoon period than during non-typhoon period, which may reflect more pronounced short-term variability of water vapor and a stronger random error component under typhoon conditions. Therefore, changes in REA-PWV performance during typhoons should be interpreted by jointly considering both systematic and random error components. When RS-PWV is used as the reference, the three REA-biases during typhoon period are overall closer to zero than those during non-typhoon period, with M-bias being the smallest, followed by E-bias, while J-bias remains relatively pronounced. For RMSE, E-RMSE and J-RMSE are lower during typhoon period than during non-typhoon period, whereas M-RMSE is broadly comparable between the two periods.

Using RO-PWV as the reference yields patterns that are not fully consistent with the ground-based evaluations. Under typhoon conditions, the three REA-biases are positive overall, and both their absolute values and RMSEs are larger than those under non-typhoon conditions. This indicates that, for the RO collocations available in this study, REA-PWVs tend to overestimate PWV relative to RO-PWV. This contrast does not contradict the GNSS-based and radiosonde-based conclusions because the RO collocations are concentrated over oceanic regions, introducing a clear land–ocean sampling difference relative to the samples used in the ground-based evaluations. Moreover, under the relatively strict collocation scheme, only 160 collocated samples are available under typhoon conditions, making the statistics more sensitive to sample composition. In terms of inter-product comparison, E-bias and M-bias are comparable under typhoon conditions, with M-bias lower by 0.15 mm, whereas J-bias is larger. For RMSE, E-RMSE is the lowest and is 1.05 mm lower than M-RMSE, while J-RMSE is the largest. Overall, these results continue to indicate the relatively robust performance of ERA5. In addition, the NSD results show enhanced local spatial variability in REA-PWV under typhoon conditions, reflecting a more complex spatial structure of the water vapor field during typhoons.

Consistent evidence from three independent references suggests that the reanalyses can provide continuous PWV information that is practically useful and reasonably reliable under typhoon conditions. Overall, ERA5 shows more consistent performance and lower error levels. JRA-3Q improves relative to non-typhoon conditions in most cases, although a systematic bias can remain in some situations. MERRA-2 tends to maintain a bias close to zero, but its uncertainty becomes more pronounced under typhoon conditions, consistent with its higher NSD and its larger increases in RMSE and NSD from non-typhoon to typhoon conditions.

This study supports the reliability and applicability of reanalysis-derived PWV under typhoon conditions and provides continuous water vapor information for typhoon monitoring and process-based analyses. It also provides a performance reference for reanalysis PWV under typhoon weather. Over oceanic regions where ground-based observations are sparse, reanalysis PWV can serve as an important reference for PWV retrieved from other technologies, facilitating product evaluation and bias diagnosis. This reference can also provide contextual information for interpreting discrepancies among different observations under typhoon conditions, thereby improving the interpretability and utility of oceanic PWV estimates in both scientific research and operational applications related to typhoons.

~~Evaluation using GNSS PWVs shows that ERA5 exhibits the most stable performance, with smallest biases and RMSE during typhoons, and slightly larger biases and errors in non-typhoon periods. While being less accurate than ERA5, JRA-3Q also has less bias and RMSE during typhoons than in non-typhoon periods, indicating that the assimilation of TCB observations has a positive contribution to PWV estimation. MERRA-2 has least accuracy in terms of RMSE. In contrast to ERA5 and JRA-3Q, its accuracy is less during typhoons compared to non-typhoon periods. Error decomposition showed that while the RMSE of MERRA-2 is the highest of the three reanalysis datasets, its bias is the smallest during non-typhoon periods, and the second smallest during typhoons. The bulk of its RMSE stems from random error components. This is likely caused by the fact that MERRA-2 shows much higher spatial variability of PWV in the neighborhoods around typhoon~~

~~tracks than ERA5 and JRA-3Q, estimated via neighborhood standard deviation. ERA5 and JRA-3Q have similar spatial variability and are thus consistent with each other.~~

~~Evaluations using RS PWVs and RO PWVs confirm the overall consistency of the three reanalyses with GNSS-based results, supporting their reliability under typhoon conditions. However, since RS and RO samples are limited, these results should be regarded as supplementary, with the GNSS-based evaluation providing the main reference.~~

~~Through a comprehensive evaluation, this study demonstrates that reanalysis data can provide continuous and reasonably reliable PWV information under typhoon conditions, even in regions where ground-based observations are sparse or unavailable. These results offer valuable references for water vapor research and practical support for typhoon monitoring and forecasting during extreme weather events. Future work will extend the evaluation to a global scale to assess the performance of various reanalysis water vapor products during TCs worldwide.~~

Data Availability

~~Typhoon information data are provided by the typhoon track real-time release system, operated by the Zhejiang provincial department of water resources and the Zhejiang water resources information management center (https://typhoon.slt.zj.gov.cn/). GNSS tropospheric products and observations are provided by IGS (https://cddis.nasa.gov/archive/gnss/products/troposphere/zpd/) and CMONOC (The authors do not have permission to share CMONOC data). COSMIC-2 RO wet profiles are provided by UCAR (https://data.cosmic.ucar.edu/gnss-ro/cosmic2). ERA5 hourly data on pressure levels is provided by ECMWF (https://cds.climate.copernicus.eu/datasets/reanalysis-era5-pressure-levels). MERRA-2 data is provided by GMAO (https://disc.gsfc.nasa.gov/datasets?project=MERRA-2). JRA-3Q data is provided by JMA (https://rda.ucar.edu/datasets/d640000/). Radiosonde data is provided by IGRA (https://www.ncei.noaa.gov/data/igra). GPM IMERG Final Precipitation L3 Half Hourly 0.1 degree x 0.1 degree V07 data is provided by JAXA and NASA (https://disc.gsfc.nasa.gov/datasets/GPM_3IMERGHH_07/summary?keywords=3IMERGHH).~~

Typhoon data are provided by the IBTrACS (https://www.ncei.noaa.gov/products/international-best-track-archive), ERA5 hourly data on pressure levels is provided by ECMWF (https://cds.climate.copernicus.eu/datasets/reanalysis-era5-pressure-levels). MERRA-2 M2I3NVASM data is provided by GMAO (https://disc.gsfc.nasa.gov/datasets?project=MERRA-2). JRA-3Q isobaric analysis fields data is provided by JMA (https://rda.ucar.edu/datasets/d640000). GNSS tropospheric products and observations are provided by IGS (https://cddis.nasa.gov/archive/gnss/products/troposphere/zpd) and CMONOC (data are available upon request and downloaded after approval). Radiosonde data is provided by IGRA (https://www.ncei.noaa.gov/data/igra). COSMIC-2 RO wet profiles are provided by UCAR (https://data.cosmic.ucar.edu/gnss-ro/cosmic2).

Author contributions

Conceptualization was carried out by JS. Data curation was performed by JS, JH, and YF. Methodology was developed by JS, MZ, and YF, with validation provided by JS and WG. Visualization was carried out by JS and JH. Formal analysis was contributed by AKS, MZ, and WG. Software support was provided by ML. Investigation was conducted by JS. Supervision was provided by ML and AKS. Writing – original draft was prepared by JS, and writing – review and editing was contributed by ML, AKS, SS, and KZ. Funding acquisition was secured by ML. All authors discussed the results, contributed to the manuscript revision, and agreed to the final version of the paper.

Competing interests

The authors declare that they have no conflict of interest.

Special issue statement

This manuscript is submitted to the special issue "The SPARC Reanalysis Intercomparison Project (S-RIP) Phase 2 (ACP/WCD inter-journal SI)".

Acknowledgments

This research was partially supported by the Special Scholarship for Graduate Students' Overseas (Outbound) Exchange Program of Wuhan University. Part of the work was carried out during my research stay at the Wegener Center for Climate and Global Change, University of Graz, Austria. The authors would also like to thank Dr. Fan Si from Physikalisches Institut der Ruprecht-Karls-Universität Heidelberg, Germany, Junyi Gao from the University of Edinburgh, UK, and Junyi Han, for their help.

Financial support

This study is supported by the Natural Science Foundation of Hubei Province, China (Grant No. 2025AFA038) and the National Natural Science Foundation of China (Grant Nos. 42474032, 42030109, 41931075, and 42004020).

References

Bell, B., Hersbach, H., Simmons, A., Berrisford, P., Dahlgren, P., Horányi, A., Muñoz-Sabater, J., Nicolas, J., Radu, R., Schepers, D., Soci, C., Villaume, S., Bidlot, J., Haimberger, L., Woollen, J., Buontempo, C., and Thépaut, J.: The

ERA5 global reanalysis: Preliminary extension to 1950, Q. J. Roy. Meteorol. Soc., 147, 4186–4227, https://doi.org/10.1002/qj.4174, 2021.

Bevis, M., Businger, S., Herring, T. A., Rocken, C., Anthes, R. A., and Ware, R. H.: GPS meteorology: Remote sensing of atmospheric water vapor using the global positioning system, J. Geophys. Res. Atmos., 97, 15787–15801, https://doi.org/10.1029/92JD01517, 1992.

Bevis, M., Businger, S., Chiswell, S., Herring, T. A., Anthes, R. A., Rocken, C., and Ware, R. H.: GPS meteorology: Mapping zenith wet delays onto precipitable water, J. Appl. Meteorol. Clim., 33, 379–386, https://doi.org/10.1175/1520-0450(1994)033%253C0379:GMMZWD%253E2.0.CO;2, 1994.

Bock, O. and Parracho, A. C.: Consistency and representativeness of integrated water vapour from ground-based GPS observations and ERA-Interim reanalysis, Atmos. Chem. Phys., 19, 9453–9468, https://doi.org/10.5194/acp-19-9453-2019, 2019.

Chan, F. K. S., Chuah, C. J., Ziegler, A. D., Dąbrowski, M., and Varis, O.: Towards resilient flood risk management for Asian coastal cities: Lessons learned from Hong Kong and Singapore, J. Cleaner Prod., 187, 576–589, https://doi.org/10.1016/j.jclepro.2018.03.217, 2018.

Cogan, J., Gratchev, I., and Wang, G.: Rainfall-induced shallow landslides caused by ex-Tropical Cyclone Debbie, 31st March 2017, Landslides, 15, 1215–1221, https://doi.org/10.1007/s10346-018-0982-4, 2018.

Davis, J. L., Herring, T. A., Shapiro, I. I., Rogers, A. E. E., and Elgered, G.: Geodesy by radio interferometry: Effects of atmospheric modeling errors on estimates of baseline length, Radio Sci., 20, 1593–1607, https://doi.org/10.1029/rs020i006p01593, 1985.

Duan, Y., Chen, L., Liang, J., Wang, Y., Wu, L., Cui, X., Ma, L., and Li, Q.: Research progress in the unusual variations of typhoons before and after landfalling, Acta Meteor. Sin., 72, 969–986, https://doi.org/10.11676/qxxb2014.085, 2014.

Elgered, G., Davis, J. L., Herring, T. A., and Shapiro, I. I.: Geodesy by radio interferometry: Water vapor radiometry for estimation of the wet delay, J. Geophys. Res.-Solid Earth, 96, 6541–6555, https://doi.org/10.1029/90jb00834, 1991.

Elsner, J. B.: Continued increases in the intensity of strong tropical cyclones, Bulletin of the American Meteorological Society, 101, E1301–E1303, https://doi.org/10.1175/BAMS-D-19-0338.1, 2020.

Emanuel, K.: Increasing destructiveness of tropical cyclones over the past 30 years, Nature, 436, 686–688, https://doi.org/10.1038/nature03906, 2005.

Esteban, M. and Longarte-Galnares, G.: Evaluation of the productivity decrease risk due to a future increase in tropical cyclone intensity in Japan: productivity decrease due to tropical cyclones, Risk Anal., 30, 1789–1802, https://doi.org/10.1111/j.1539-6924.2010.01483.x, 2010.

Gahtan, J., Knapp, K. R., Schreck, C. J. I., Diamond, H. J., Kossin, J. P., and Kruk, M. C.: International Best Track Archive for Climate Stewardship (IBTrACS) project, version 4.01 (Version 4r01), https://doi.org/10.25921/82ty-9e16, 2024.

Gelaro, R., McCarty, W., Suárez, M. J., Todling, R., Molod, A., Takacs, L., Randles, C. A., Darmenov, A., Bosilovich, M. G., Reichle, R., Wargan, K., Coy, L., Cullather, R., Draper, C., Akella, S., Buchard, V., Conaty, A., Da Silva, A. M.,

Gu, W., Kim, G.-K., Koster, R., Lucchesi, R., Merkova, D., Nielsen, J. E., Partyka, G., Pawson, S., Putman, W., Rienecker, M., Schubert, S. D., Sienkiewicz, M., and Zhao, B.: The modern-era retrospective analysis for research and applications, version 2 (MERRA-2), J. Climate, 30, 5419–5454, https://doi.org/10.1175/JCLI-D-16-0758.1, 2017.

Gui, K., Che, H., Chen, Q., Zeng, Z., Liu, H., Wang, Y., Zheng, Y., Sun, T., Liao, T., Wang, H., and Zhang, X.: Evaluation of radiosonde, MODIS-NIR-Clear, and AERONET precipitable water vapor using IGS ground-based GPS measurements over China, Atmos. Res., 197, 461–473, https://doi.org/10.1016/j.atmosres.2017.07.021, 2017.

Hersbach, H., Bell, B., Berrisford, P., Hirahara, S., Horányi, A., Muñoz-Sabater, J., Nicolas, J., Peubey, C., Radu, R., Schepers, D., Simmons, A., Soci, C., Abdalla, S., Abellan, X., Balsamo, G., Bechtold, P., Biavati, G., Bidlot, J., Bonavita, M., De Chiara, G., Dahlgren, P., Dee, D., Diamantakis, M., Dragani, R., Flemming, J., Forbes, R., Fuentes, M., Geer, A., Haimberger, L., Healy, S., Hogan, R. J., Hólm, E., Janisková, M., Keeley, S., Laloyaux, P., Lopez, P., Lupu, C., Radnoti, G., De Rosnay, P., Rozum, I., Vamborg, F., Villaume, S., and Thépaut, J.: The ERA5 global reanalysis, Q. J. Roy. Meteorol. Soc., 146, 1999–2049, https://doi.org/10.1002/qj.3803, 2020.

Holloway, C. E. and Neelin, J. D.: Moisture vertical structure, column water vapor, and tropical deep convection, J. Atmos. Sci., 66, 1665–1683, https://doi.org/10.1175/2008JAS2806.1, 2009.

Ichoku, C., Levy, R., Kaufman, Y. J., Remer, L. A., Li, R., Martins, V. J., Holben, B. N., Abuhassan, N., Slutsker, I., Eck, T. F., and Pietras, C.: Analysis of the performance characteristics of the five-channel Microtops II Sun photometer for measuring aerosol optical thickness and precipitable water vapor, J. Geophys. Res. Atmos., 107, 4179, https://doi.org/10.1029/2001jd001302, 2002.

Johnston, B. R., Randel, W. J., and Sjoberg, J. P.: Evaluation of tropospheric moisture characteristics among COSMIC-2, ERA5 and MERRA-2 in the tropics and subtropics, Remote Sens., 13, 880, https://doi.org/10.3390/rs13050880, 2021.

Jung, K., Kam, J., and Lee, S.: Tropical cyclone risk assessment reflecting the climate change trend: the case of South Korea, Nat. Hazards, 120, 5841–5867, https://doi.org/10.1007/s11069-024-06428-0, 2024.

King, M. D., Menzel, W. P., Kaufman, Y. J., Tanre, D., Bo-Cai Gao, Platnick, S., Ackerman, S. A., Remer, L. A., Pincus, R., and Hubanks, P. A.: Cloud and aerosol properties, precipitable water, and profiles of temperature and water vapor from MODIS, IEEE Trans. Geosci. Remote Sens., 41, 442–458, https://doi.org/10.1109/tgrs.2002.808226, 2003.

Knapp, K. R., Kruk, M. C., Levinson, D. H., Diamond, H. J., and Neumann, C. J.: The International Best Track Archive for Climate Stewardship (IBTrACS): Unifying tropical cyclone data, Bull. Amer. Meteor. Soc., 91, 363–376, https://doi.org/10.1175/2009BAMS2755.1, 2010.

Knutson, T., Camargo, S. J., Chan, J. C. L., Emanuel, K., Ho, C.-H., Kossin, J., Mohapatra, M., Satoh, M., Sugi, M., Walsh, K., and Wu, L.: Tropical cyclones and climate change assessment: Part II: Projected response to anthropogenic warming, B. Am. Meteorol. Soc., 101, E303–E322, https://doi.org/10.1175/BAMS-D-18-0194.1, 2020.

Kosaka, Y., Kobayashi, S., Harada, Y., Kobayashi, C., Naoe, H., Yoshimoto, K., Harada, M., Goto, N., Chiba, J., Miyaoka, K., Sekiguchi, R., Deushi, M., Kamahori, H., Nakaegawa, T., Tanaka, T. Y., Tokuhiro, T., Sato, Y., Matsushita, Y., and Onogi, K.: The JRA-3Q reanalysis, J. Meteor. Soc. Japan, 102, 49–109, https://doi.org/10.2151/jmsj.2024-004, 2024.

Kossin, J. P.: A global slowdown of tropical-cyclone translation speed, Nature, 558, 104–107, https://doi.org/10.1038/s41586-018-0158-3, 2018.

Kursinski, E. R., Hajj, G. A., Bertiger, W. I., Leroy, S. S., Meehan, T. K., Romans, L. J., Schofield, J. T., McCleese, D. J., Melbourne, W. G., Thornton, C. L., Yunck, T. P., Eyre, J. R., and Nagatani, R. N.: Initial results of radio occultation observations of Earth's atmosphere using the Global Positioning System, Science, 271, 1107–1110, https://doi.org/10.1126/science.271.5252.1107, 1996.

Li, M., Li, W., Shi, C., Jiang, K., Guo, X., Dai, X., Meng, X., Yang, Z., Yang, G., and Liao, M.: Precise orbit determination of the Fengyun-3C satellite using onboard GPS and BDS observations, J. Geodesy, 91, 1313–1327, https://doi.org/10.1007/s00190-017-1027-9, 2017.

Li, W., Yao, Y., Zhang, L., Peng, W., Du, Z., Zuo, Y., and Wang, W.: Evaluating global precipitable water vapor products from four public reanalysis using radiosonde data, Geod. Geodyn., 16, 693–705, https://doi.org/10.1016/j.geog.2025.02.007, 2025.

Li, Z., Muller, J., and Cross, P.: Comparison of precipitable water vapor derived from radiosonde, GPS, and moderate-resolution imaging spectroradiometer measurements, J. Geophys. Res. Atmos., 108, 2003JD003372, https://doi.org/10.1029/2003JD003372, 2003.

Melbourne, W. G., Davis, E. S., Duncan, C. B., Hajj, G. A., Hardy, K. R., Kursinski, E. R., Meehan, T. K., Young, L. E., and Yunck, T. P.: The application of spaceborne GPS to atmospheric limb sounding global change monitoring, Jet Propulsion Laboratory, California Institute of Technology, 1994.

Muller, C. J., Back, L. E., O'Gorman, P. A., and Emanuel, K. A.: A model for the relationship between tropical precipitation and column water vapor, Geophys. Res. Lett., 36, L16804, https://doi.org/10.1029/2009GL039667, 2009.

Pérez-Ramírez, D., Whiteman, D. N., Smirnov, A., Lyamani, H., Holben, B. N., Pinker, R., Andrade, M., and Alados-Arboledas, L.: Evaluation of AERONET precipitable water vapor versus microwave radiometry, GPS, and radiosondes at ARM sites, J. Geophys. Res. Atmos., 119, 9596–9613, https://doi.org/10.1002/2014jd021730, 2014.

Rani, S. and Singh, J.: Evaluation of MODIS, ERA5, and MERRA2 derived integrated precipitable water vapor of India using ground-based GPS data, Ann. Am. Assoc. Geogr., 115, 1506–1531, https://doi.org/10.1080/24694452.2025.2493823, 2025.

Saastamoinen, J.: Atmospheric correction for the troposphere and stratosphere in radio ranging satellites, in: The Use of Artificial Satellites for Geodesy, 247–251, https://doi.org/10.1029/GM015p0247, 1972.

Schneider, T., O'Gorman, P. A., and Levine, X. J.: Water vapor and the dynamics of climate changes, Rev. Geophys., 48, RG3001, https://doi.org/10.1029/2009rg000302, 2010.

Schreiner, W. S., Weiss, J. P., Anthes, R. A., Braun, J., Chu, V., Fong, J., Hunt, D., Kuo, Y. -H., Meehan, T., Serafino, W., Sjoberg, J., Sokolovskiy, S., Talaat, E., Wee, T. K., and Zeng, Z.: COSMIC-2 radio occultation constellation: First results, Geophys. Res. Lett., 47, e2019GL086841, https://doi.org/10.1029/2019gl086841, 2020.

Sherwood, S. C., Roca, R., Weckwerth, T. M., and Andronova, N. G.: Tropospheric water vapor, convection, and climate, Rev. Geophys., 48, RG2001, https://doi.org/10.1029/2009rg000301, 2010.

Shi, C., Zhao, Q., Geng, J., Lou, Y., Ge, M., and Liu, J.: Recent development of PANDA software in GNSS data processing, International Conference on Earth Observation Data Processing and Analysis (ICEODPA), https://doi.org/10.1117/12.816261, 2008.

Shi, C., Zhou, L., Fan, L., Zhang, W., Cao, Y., Wang, C., Xiao, F., Lv, G., and Liang, H.: Analysis of "21·7" extreme rainstorm process in Henan Province using BeiDou/GNSS observation, China J. Geophys., 65, 186–196, https://doi.org/10.6038/cjg2022P0706, 2022.

Shi, J., Zhang, K., Wu, S., Shi, S., and Shen, Z.: Investigation of the atmospheric boundary layer height using radio occultation: a case study during twelve super typhoons over the northwest Pacific, Atmosphere, 12, 1457, https://doi.org/10.3390/atmos12111457, 2021.

Shi, J., Li, M., Steiner, A. K., Li, W., Zhang, M., Fan, Y., Gao, W., and Zhang, K.: Stacking machine learning model for precipitable water vapor vertical adjustment using GNSS networks and radio occultation data, Atmos. Res., 325, 108212, https://doi.org/10.1016/j.atmosres.2025.108212, 2025.

Soci, C., Hersbach, H., Simmons, A., Poli, P., Bell, B., Berrisford, P., Horányi, A., Muñoz-Sabater, J., Nicolas, J., Radu, R., Schepers, D., Villaume, S., Haimberger, L., Woollen, J., Buontempo, C., and Thépaut, J.: The ERA5 global reanalysis from 1940 to 2022, Q. J. Roy. Meteorol. Soc., 150, 4014–4048, https://doi.org/10.1002/qj.4803, 2024.

Turner, D. D., Lesht, B. M., Clough, S. A., Liljegren, J. C., Revercomb, H. E., and Tobin, D. C.: Dry bias and variability in Vaisala RS80-H radiosondes: The ARM experience, J. Atmos. Oceanic Technol., 20, 117–132, https://doi.org/10.1175/1520-0426(2003)020%253C0117:dbaviv%253E2.0.co;2, 2003.

Turner, D. D., Clough, S. A., Liljegren, J. C., Clothiaux, E. E., Cady-Pereira, K. E., and Gaustad, K. L.: Retrieving liquid water path and precipitable water vapor from the Atmospheric Radiation Measurement (ARM) microwave radiometers, IEEE Trans. Geosci. Remote Sens., 45, 3680–3690, https://doi.org/10.1109/tgrs.2007.903703, 2007.

Utsumi, N. and Kim, H.: Observed influence of anthropogenic climate change on tropical cyclone heavy rainfall, Nat. Clim. Chang., 12, 436–440, https://doi.org/10.1038/s41558-022-01344-2, 2022.

Vey, S., Dietrich, R., Rülke, A., Fritsche, M., Steigenberger, P., and Rothacher, M.: Validation of precipitable water vapor within the NCEP/DOE reanalysis using global GPS observations from one decade, J. Climate, 23, 1675–1695, https://doi.org/10.1175/2009JCLI2787.1, 2010.

Walsh, K. J. E., McInnes, K. L., and McBride, J. L.: Climate change impacts on tropical cyclones and extreme sea levels in the South Pacific—A regional assessment, Glob. Planet. Chang., 80–81, 149–164, https://doi.org/10.1016/j.gloplacha.2011.10.006, 2012.

Wang, J. and Zhang, L.: Systematic errors in global radiosonde precipitable water data from comparisons with ground-based GPS measurements, J. Climate, 21, 2218–2238, https://doi.org/10.1175/2007JCLI1944.1, 2008.

Wang, J., Zhang, L., and Dai, A.: Global estimates of water-vapor-weighted mean temperature of the atmosphere for GPS applications, J. Geophys. Res. Atmos., 110, D21101, https://doi.org/10.1029/2005jd006215, 2005.

Wang, L., Zhou, Y., Lei, X., Zhou, Y., Bi, H., and Mao, X.: Predominant factors of disaster caused by tropical cyclones in South China coast and implications for early warning systems, Sci. Total Environ., 726, 138556, https://doi.org/10.1016/j.scitotenv.2020.138556, 2020a.

Wang, S., Xu, T., Nie, W., Jiang, C., Yang, Y., Fang, Z., Li, M., and Zhang, Z.: Evaluation of precipitable water vapor from five reanalysis products with ground-based GNSS observations, Remote Sens., 12, 1817, https://doi.org/10.3390/rs12111817, 2020b.

Wang, S., Xu, T., Xu, Y., Jiang, C., Gao, F., Zhang, Z., Yang, Y., Fang, Z., and Xue, H.: Intercomparison of total precipitable water derived from COSMIC-2 and three different microwave radiometers over the ocean, IEEE Trans. Geosci. Remote Sens., 60, 4107610, https://doi.org/10.1109/TGRS.2022.3160020, 2022.

Wang, Y., Yang, K., Pan, Z., Qin, J., Chen, D., Lin, C., Chen, Y., Lazhu, Tang, W., Han, M., Lu, N., and Wu, H.: Evaluation of precipitable water vapor from four satellite products and four reanalysis datasets against GPS measurements on the southern Tibetan Plateau, J. Climate, 30, 5699–5713, https://doi.org/10.1175/JCLI-D-16-0630.1, 2017.

Wang, Z.: Role of cumulus congestus in tropical cyclone formation in a high-resolution numerical model simulation, J. Atmos. Sci., 71, 1681–1700, https://doi.org/10.1175/JAS-D-13-0257.1, 2014.

Wang, Z. and Hankes, I.: Moisture and precipitation evolution during tropical cyclone formation as revealed by the SSM/I–SSMIS retrievals, J. Atmos. Sci., 73, 2773–2781, https://doi.org/10.1175/JAS-D-15-0306.1, 2016.

Wang, Z., Xia, N., Zhao, X., Ji, X., and Wang, J.: Comprehensive risk assessment of typhoon disasters in China's coastal areas based on multi-source geographic big data, Sci. Total Environ., 926, 171815, https://doi.org/10.1016/j.scitotenv.2024.171815, 2024.

Wee, T.-K., Anthes, R. A., Hunt, D. C., Schreiner, W. S., and Kuo, Y.-H.: Atmospheric GNSS RO 1D-Var in use at UCAR: Description and validation, Remote Sens., 14, 5614, https://doi.org/10.3390/rs14215614, 2022.

Wei, Q., Xingdong Li, Ma, T., Wang, S., Tiantian Dai, Peng Fan, Yunhan Yu, Yongjie Jin, and Liu, Y.: A neighborhood standard deviation based algorithm for generating PET crystal position maps, in: 2013 IEEE Nuclear Science Symposium and Medical Imaging Conference (2013 NSS/MIC), 2013 IEEE Nuclear Science Symposium and Medical Imaging Conference (2013 NSS/MIC), 1–4, https://doi.org/10.1109/nssmic.2013.6829273, 2013.

Woodruff, J. D., Irish, J. L., and Camargo, S. J.: Coastal flooding by tropical cyclones and sea-level rise, Nature, 504, 44–52, https://doi.org/10.1038/nature12855, 2013.

Xi, D., Lin, N., and Gori, A.: Increasing sequential tropical cyclone hazards along the US East and Gulf coasts, Nat. Clim. Chang., 13, 258–265, https://doi.org/10.1038/s41558-023-01595-7, 2023.

Yuan, P., Blewitt, G., Kreemer, C., Jiang, W., Liu, T., He, L., Shan, Q., Balidakis, K., Schuh, H., Wickert, J., and Deng, Z.: A global assessment of diurnal discontinuities in ERA5 tropospheric zenith total delays using 10 years of GNSS data, Geophys. Res. Lett., 52, e2024GL113140, https://doi.org/10.1029/2024GL113140, 2025.

Zhang, C., Wang, S., Zhao, Y., Xu, Y., Zhang, J., Mo, Y., and Yu, H.: Evaluation of water vapor from CARRA reanalysis based on GNSS and radiosonde observation in the Arctic, J. Atmos. Sol-terr. Phy., 268, 106431, https://doi.org/10.1016/j.jastp.2025.106431, 2025.

Zhang, K., Li, H., Wang, X., Zhu, D., He, Q., Li, L., Hu, A., Zheng, N., and Li, H.: Recent progresses and future prospectives of ground-based GNSS water vapor sounding, Acta Geod. Cartogr. Sin., 51, 1172–1191, https://doi.org/10.11947/j.AGCS.2022.20220149, 2022.

Zhang, Q., Ye, J., Zhang, S., and Han, F.: Precipitable water vapor retrieval and analysis by multiple data sources: Ground-based GNSS, radio occultation, radiosonde, microwave satellite, and NWP reanalysis data, J. Sensors, 2018, 1–13, https://doi.org/10.1155/2018/3428303, 2018.

Zhang, W., Lou, Y., Haase, J. S., Zhang, R., Zheng, G., Huang, J., Shi, C., and Liu, J.: The use of ground-based GPS precipitable water measurements over China to assess radiosonde and ERA-Interim moisture trends and errors from 1999 to 2015, J. Climate, 30, 7643–7667, https://doi.org/10.1175/JCLI-D-16-0591.1, 2017.

Zhang, W., Zhang, H., Liang, H., Lou, Y., Cai, Y., Cao, Y., Zhou, Y., and Liu, W.: On the suitability of ERA5 in hourly GPS precipitable water vapor retrieval over China, J. Geodesy, 93, 1897–1909, https://doi.org/10.1007/s00190-019-01290-6, 2019a.

Zhang, Y., Cai, C., Chen, B., and Dai, W.: Consistency evaluation of precipitable water vapor derived from ERA5, ERA-Interim, GNSS, and radiosondes over China, Radio Sci., 54, 561–571, https://doi.org/10.1029/2018RS006789, 2019b.

Zhao, D., Xu, H., Li, Y., Yu, Y., Duan, Y., Xu, X., and Chen, L.: Locally opposite responses of the 2023 Beijing–Tianjin–Hebei extreme rainfall event to global anthropogenic warming, npj Clim. Atmos. Sci., 7, https://doi.org/10.1038/s41612-024-00584-7, 2024.

Zhao, Q., Ma, X., Yao, W., Liu, Y., and Yao, Y.: A drought monitoring method based on precipitable water vapor and precipitation, J. Climate, 33, 10727–10741, https://doi.org/10.1175/jcli-d-19-0971.1, 2020.

Zumberge, J. F., Heflin, M. B., Jefferson, D. C., Watkins, M. M., and Webb, F. H.: Precise point positioning for the efficient and robust analysis of GPS data from large networks, J. Geophys. Res.-Solid Earth, 102, 5005–5017, https://doi.org/10.1029/96jb03860, 1997.